Master thesis

Search for linear-chain cluster states in ^{14}C

Center for Nuclear Study, Graduate School of Science, University of Tokyo

Yuji Sakaguchi

February 4, 2016

Contents

List of Tables

List of Figures

Abstract

Despite a long history of study for linear-chain cluster states, there is no clear evidence of the states. Suhara and En'yo predicted that the linear-chain cluster levels comprise a rotational band in ^{14}C. The resonant parameters such as J^{π} and α width in ^{14}C have not been studied well. In order to search for the linear-chain cluster states and determine the resonant parameters in ^{14}C, a measurement of ^{10}Be+α resonant elastic scattering was performed in 2015. The ^{10}Be beam was generated with CRIB. Thick target method in inverse kinematics was used with He gas being treated as the target. In order to eliminate events of contamination and select only ^{10}Be+α resonant elastic scattering events, an analysis was performed, and an excitation function was obtained. We observed candidates of the resonances, and compared the excitation function with results of previous measurements. There is a possibility that the candidates are of linear-chain cluster levels.

Chapter 1

Introduction

1.1 Background

1.1.1 Background of linear-chain cluster states

In nuclear astrophysics, the triple-alpha process is considered as very important. ^{12}C is created via the process and the ^{12}C is excited to the Hoyle state. This state has been investigated theoretically and experimentally. Recently the α cluster model is considered as a powerful tool to study nuclear clustering, and nuclides are known to form α cluster states at certain situations.Linear-chain α cluster states are especially considered as exotic and interesting. Such states have been theoretically investigated for a long time, but there is no clear evidence for the existence of those states.

Morinaga [1] suggested that the Hoyle state in ^{12}C corresponded to the configuration where 3 α particles are aligned in a line. Horiuchi [2, 3] pointed out that the Hoyle state could be a molecular-like level of ^{8}Be+α, or 3 α particles being coupled with that state by orthogonality condition model (OCM). Uegaki et al [4] investigated the configuration with generator coordinate method (GCM), Fukushima and Kamimura [5, 6] investigated the configuration with resonating group method (RGM), and their theoretical investigations were concluded as similar results. The idea of the linear chain was revived by Kato et al. [7], and it was suggested that the third 0^+ state has a large fraction of overlap with the linear-chain configuration by using the OCM calculation. Other calculations have been performed as well. En'yo obtained level energies and transition strength, B(E2) values by using antisymmetrized molecular dynamics (AMD) framework [8]. Tohsaki [9] explained that the Hoyle state has a dilute-cluster structure, where 3 α particles weakly interact and those α particles are condensed in the lowest s orbit. The third 0^+ state was described as the bending cluster state by Neff and Feldmeier [10] with fermionic molecular dynamic (FMD) calculation. For other

isotopes of carbon, Itagaki et al. [11, 12] discussed linear-chain states in ^{12,14,16}C by using a microscopic model. They investigated breathing and bending motions, and concluded that ^{16}C has a stable linear-chain state at the excitation energy $E_{\rm ex}$ above 20 MeV. In the following work, they discussed an equilateral-triangular structure emerging in ^{14}C. These structures should correspond to the rotational band of K^π, component of the J^π projected to an axis of symmetry, = 3^-. The first members of the band are the states at $E_{\rm ex}$ = 9.80 MeV state and 11.67 MeV (4^-). Oertzen et al. [13] mentioned that the prolate $K = 0^\pm$ band in ^{14}C as shown in Figure 1.1 is derived from the linear-chain structure. However the reason was based only on the relatively high momentum of inertia, and the values of J^π were determined only at the low energy region. Hence clear evidence of the existence of the linear-chain cluster state has not been suggested yet.

Suhara and En'yo [14, 15] obtained a band ($0_5{}^+$, $2_6{}^+$, $4_6{}^+$) which could be explained as linear-chain cluster levels. They predicted that these levels appear some MeV or more above the threshold of ^{10}Be+α. Figure 1.2 shows the proton and neutron densities in AMD wave function of a prolate-deformed state. The 0^+ state has a overlap of 64 % with this wave function. The investigation of Suhara and En'yo suggeted that the AMD wave function has a configuration as in Figure 1.2. This implies that it could be possible to access linear chain states by ^{10}Be+α channel.

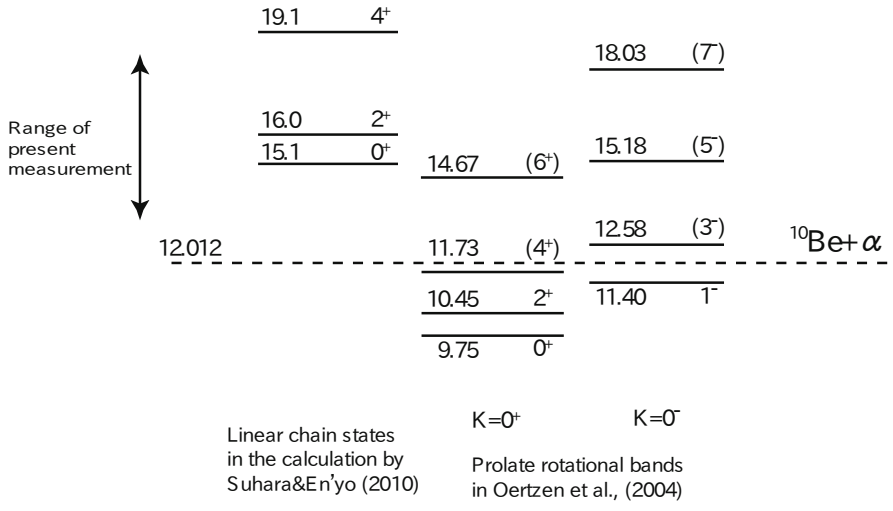

Figure 1.1: Energies of levels in the prolate K=$0^\pm$ bands suggested by Oertzen et al [13]. are shown in the middle column and the right column. The linear-chain levels in calculation by Suhara and En'yo [14, 15] are shown in the left column.

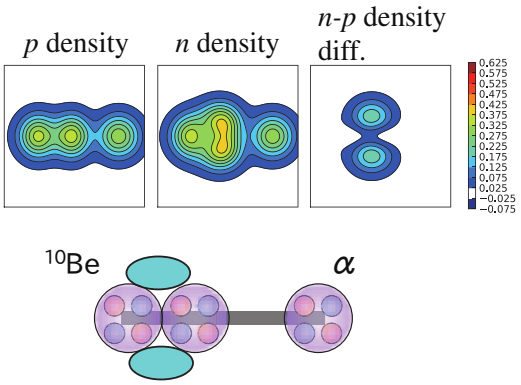

Figure 1.2: AMD wave function calculated by Suhara and En'yo. Pictures in the top side show the proton density, the neutron density and the difference of them. Picture of the bottom side shows the intuitive configuration deduced from the densities.

1.1.2 Experimental data of ^{14}C

The excited states in ^{14}C have been investigated with many reactions. Some investigations are motivated by interest for the cluster states of ^{14}C and performed with ^{7}Li(^{9}Be,^{14}C*)d [16], 2n-transfer [13], ^{12}C(^{6}He,α)^{14}C [17], ^{14}C(^{13}C,^{14}C*) [18], ^{14}C(^{14}C,^{14}C*) [19], and ^{12}C(^{16}O,^{14}O)^{14}C* [20]. Table 1.1 shows resonances in ^{14}C measured by methods which were considered to have better sensitivity for α cluster states. As Table 1.1 shows some resonances were measured, but only energies were determined. In order to discuss the structure precisely, the parameters of J$^{\pi}$ and α width should be determined.

In 2014, Freer et al [21]. observed the resonances in ^{14}C with ^{10}Be+α elastic resonant scattering, and determined the resonant parameters such as J^{π} and α width. However the energy region where the resonant parameters were determined was only at 16.5-22 MeV. The energy region at which Suhara and En'yo predicted that there are the linear-chain cluster states was around 15-19 MeV. Hence there are still resonant parameters which should be determined.

1.2 Purpose

1.2.1 Purpose of this experiment

There were 2 important goals of this experiments.

J^π		E_{ex} (MeV)					
[22]	[20]	[22]	[16]	[17]	[18]	[19]	[20]
(3^-)	$(0^-,2^-,3^-)$	12.963		13.0			12.96
						14.3	14.1
(4^+)	(5^-)	14.667	14.7		14.9	14.8	14.87
(3^-)		15.44	15.5	15.6		15.6	15.75
(4^+)		16.02			15.9		
		16.43	16.4	16.5	16.5	16.4	16.72
(4^-)		17.3				17.3	17.5
	$(2^-,4^-,6^-)$	18.5	18.5	18.5	18.5	18.6	18.6
					(19.1)	(19.0)	
			19.8	19.7	(19.9)	(19.8)	
		20.4	20.6			20.6	

Table 1.1: Resonances at 12.9-20.6 MeV in ^{14}C possibly have a large α width, observed with previous measurements.

Finding the linear-chain cluster states was the first purpose. Such states have been studied for a long time as explained above. However there is no clear evidence of existence of the linear-chain cluster states. If the existence is proved, it is a big impact for the cluster study.

Determining the resonant parameters such as J^π and α width was the second purpose. ^{14}C have been investigated with many reactions, and the level energies have been determined. However most of the resonant parametes are not determined. If the resonant parameters are determined, the precise discussion for the structure of the ^{14}C is possible.

1.2.2 Work of this paper

Especially as work of this paper, the excitation function of ^{14}C was measured, and that was compared with the previous measurements which have been investigated for the α-cluster structure of ^{14}C.

Chapter 2

Method

2.1 Reaction for the purpose of this experiment

In order to meet the purpose of this experiment, we used the elastic resonant scattering between ^{10}Be and α. There are 3 reasons for choosing this method. Firstly, by considering the intuitive picture shown in Figure 1.2, it is possible to access the linear-chain cluster state via ^{10}Be+α scattering. Secondly, to measure the α-cluster states selectively is possible. Thirdly, analysis to determine the resonant parameters becomes simple, since ^{10}Be (ground state) and α are both $J^{\pi}=0^{+}$ particles. That implies the resonant shape of the elastic scattering is determined solely by the angular momentum which directly corresponds to the spin of the resonant state.

2.2 Thick Target Method in Inverse Kinematics

Thick target method [23] in inverse kinematics method was used. In the traditional method, comparably light nuclei such as α are used as beams. In this method covering the wide region of excitaion energy in comparably narrow step is laborious. In addition, study is difficult when it is necessary to use rare isotopes.

In the present method, the geometry is inverse to the traditional experimental geometry. A beam of heavy ions is accelerated in a cyclotron enters into a reaction chamber filled with target gas such as helium. By using heavy ions as a beam, measurements of reactions with radioactive isotopes are possible. The gas serves as a target, a moderater and a shield. Heavy ions react with particles in the gas. The gas decreases the beam energy by the electric effect, and the reactions occur not only at only one energy but at a certain energy region with only a single incident energy. The gas stops the beam before the beam reaches a detector. Therefore it is possible to measure at 0 degree. At 0 degree, the potential scatttering is the

minimum and the resonant scattering is the maximum.

Summarizing the advantages of the thick target method in inverse kinematics is as follows

- Measurement is possible for short-lived RI which can not be used as the target.
- It is possible to measure simultaneously at a certain energy range with a single initial beam energy.
- The beam can be stopped in the target, and a measurement is possible at θ_{cm}, angle in center-of-mass system, =180 degree (where the potential scattering is minimal, and resonant scattering is maximal).

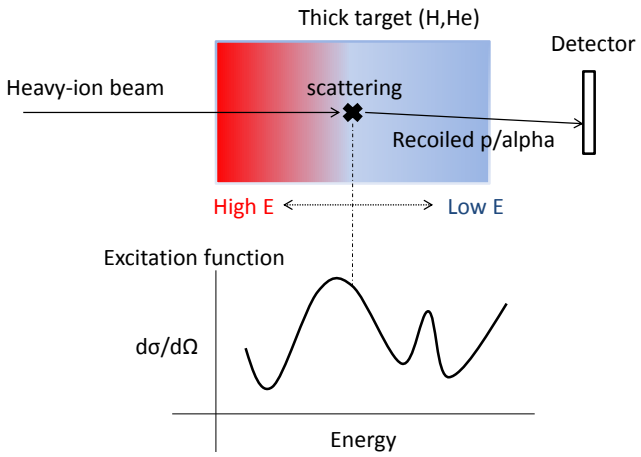

Figure 2.1: Diagram of a concept of Thick target method in inverse kinematics. The heavy-ion beam enters into the thick target. The reaction of scattering occurs with the beam passing through the target as the beam energy is decreased. The recoiled light particle is detected, and the excitation function is constructed without changing the beam energy. The possibility to scan a certain energy region with a single incident energy is shown.

2.3 CRIB

In order to measure the ^{10}Be+α elastic resonant scattering with the thick target method in inverse kinematics, we used CNS RadioIsotope Beam Separator (CRIB) [24]. CRIB is a in-flight low-energy RI beam separator. CRIB is operated by Center for Nuclear Study, University of Tokyo (CNS), and located in the Nishina Center of RIKEN. The Electron Cyclotron Resonance ion source (ECR) and the K70 Azimuthally Varying Field (AVF) cyclotron provide high-intensity heavy ion beam up to 10 MeV/u if A/Z is over 2. Most of the RI beams are generated by two-body reactions such as (p,n), (d,p) and (^{3}He,d) in inverse kinematics. CRIB is composed of two parts. One is the double achromatic system including Q1 M1 D1 Q2 D2 M2 and Q3 shown in 2.2. The other is Wien filter system including Q4 Q5 $\vec{E} \times \vec{B}$ Q6 Q7. Here Q denotes quadrapole magnets, M multipole magnets, D dipole magnets and $\vec{E} \times \vec{B}$ velocity filters. The particles in the secondary beam which has momentum of p and charge of q are separated by the double achromatic system as $B\rho$=p/q. After that those particles separated by the Wien filter as the velocity of v which satisfies the Lorentz force equation, $qE = qvB$.

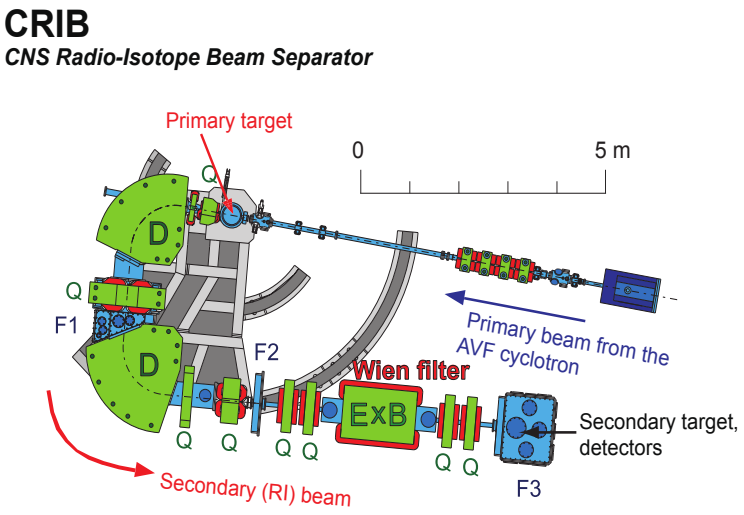

Figure 2.2: Overview of CRIB.

2.4 Generating ^{10}Be

Table 2.1 shows parameters to generate the ^{10}Be beam, used in this experiment. The primary beam was $^{11}B^{3+}$. The energy was 5.1 MeV/u. The production reaction was ^{11}B(d,^{3}He)^{10}Be. Deuteron gas was used as the production target. The deuteron gas was filled in the target cell of which length was 80 mm at the F0 focal plane. The pressure was 500 Torr. After generating ^{10}Be in the F0 chamber, we selected ^{10}Be beam among the secondary beams.

Firstly the Bρ separation was performed by double achromatic system for excluding contamination. The Bρ of the D1 magnet was chosen so that the intensity of the beam which passed through the center of the F1 focal plane was the largest. We used a degrader of a 1.2 μm Mylar foil in the F1 chamber in order to exclude contamination. Particles lost energy depending on their kind of ion with the degrader at F1. $B\rho$ of the D2 magnet was set so that only the ^{10}Be enters into the center of the F2 focal plane.

Secondary, Wien filter was used in order to exclude contamination. The voltages of the Wien filter were set so that only the ^{10}Be beam reached the reaction chamber (a chamber for the reaction of ^{10}Be+α elastic resonant scattering.)

Energy of ^{11}B	5.1 MeV/u
Intensity of ^{11}B	2.0 eμA
Target (deuteron gas) pressure	500 Torr
Target (deuteron gas) thickness	80 mm
D1 $B\rho$	0.68512 Tm
F1 degrader	1.2 μm Mylar foil
D2 $B\rho$	0.68315 Tm
Wien filter positive voltage	+57 kV
Wien filter negative voltage	-57 kV

Table 2.1: Values used at this experiment

The purity of the ^{10}Be was around 94 %. The contaminations were α, $^{6}Li^{3+}$ and $^{7}Li^{3+}$ particles. The F3 chamber was used as the reaction chamber. The intensity of the ^{10}Be beam which reached the reaction chamber was around 1.8 x 10^4 cps.

2.5 Setup

2.5.1 Reaction chamber setup

Figure 2.3 shows the top view of the reaction chamber. Figure 2.4 is the picture of the situation inside the reaction chamber. We used Parallel-Plate Avalanche Counter (PPAC) [25]. There were PPACa and PPACb, measuring the position, the timing and the count of the beam was possible. This information was used in order to identify the ^{10}Be. The extrapolation of the beam was also performed to eliminate events in which the beam did not enter into the reaction chamber. This analysis is discussed in Chapter 3.

We used 2 telescopes, a set of detectors. The first telescope was installed on the beam line (centered). The second telescope was installed and it was angled. The two telescopes were laid on a plastic sheet of which shape was a sector which was hollowed by a smaller sector. The second angled telescope faced the center of the sector and the angle was 12.5 degrees. The distance from the entrance window to the center was 240.5 mm. The distance from the window to the centered telescope was 555 mm. The reaction chamber was sealed with a 20 μm Mylar foil, and filled with He gas. The pressure was 700 Torr. The He gas worked as the thick target. These pressure and the distance were set for the beam to stop in front of the centered telescope. In this paper, z direction is defined as the beam traveling direction, the x direction is defined as the horizontal direction, and the y direction is defined as the vertical direction.

2.5.2 Telescope

Two telescope were used in this experiment. The telescopes were composed of a 20 μm thin Si detector and a 480 μm thick Si detector. The thin detector was set on the upstream side, and the thick detector was on the downstream side. Figure 2.5 shows the telescope setup. In order to measure the energy, the position, and the timing of the particle, Position-Sensitive Detectors (PSDs) [26] were used. The explanation about the PSD is written below.

The purpose of using the 2 layer was to identify α particles in a plot of total energies (E) versus deposited energies (Δ E). The first detector was thin sufficiently for target ions to pierce. ΔE was the deposited energy in the first thin detector. The quantity of the deposited energy depended on the nuclide. Hence even though the total energy of the particles were same, the deposited energies in the first thin detector were different depending on the nuclides. Particles had their loci in the ΔE and E plot according to their nuclides, and α particles also had their own locus. It was possible to eliminate events of contamination by selecting the locus of the α particles (shown in Figure 2.6). Details of a method of selecting α

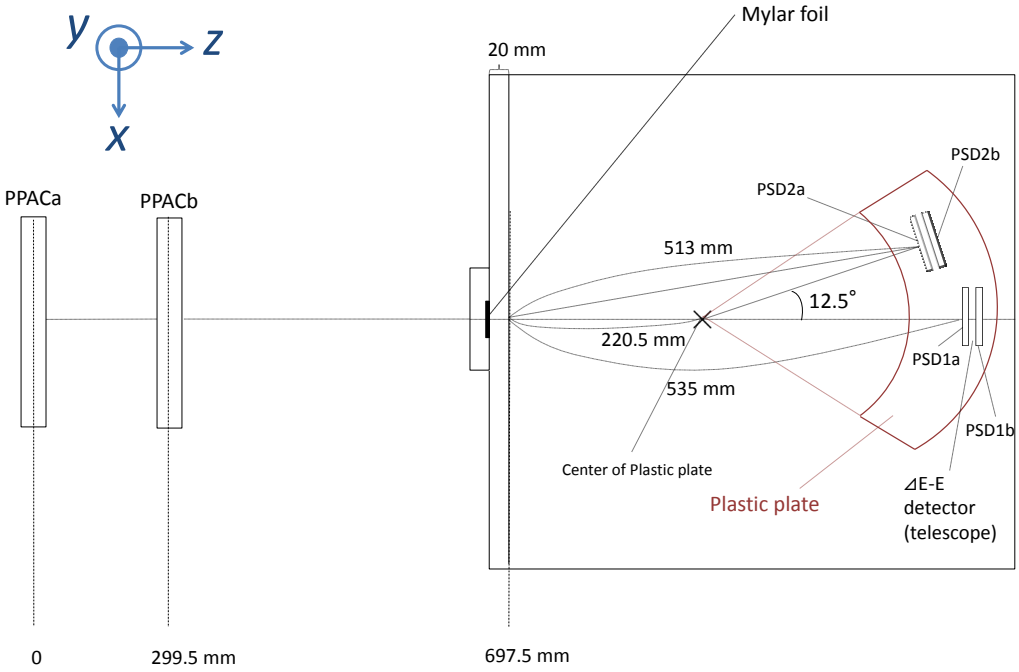

Figure 2.3: Top view of our setup in the reaction chamber.

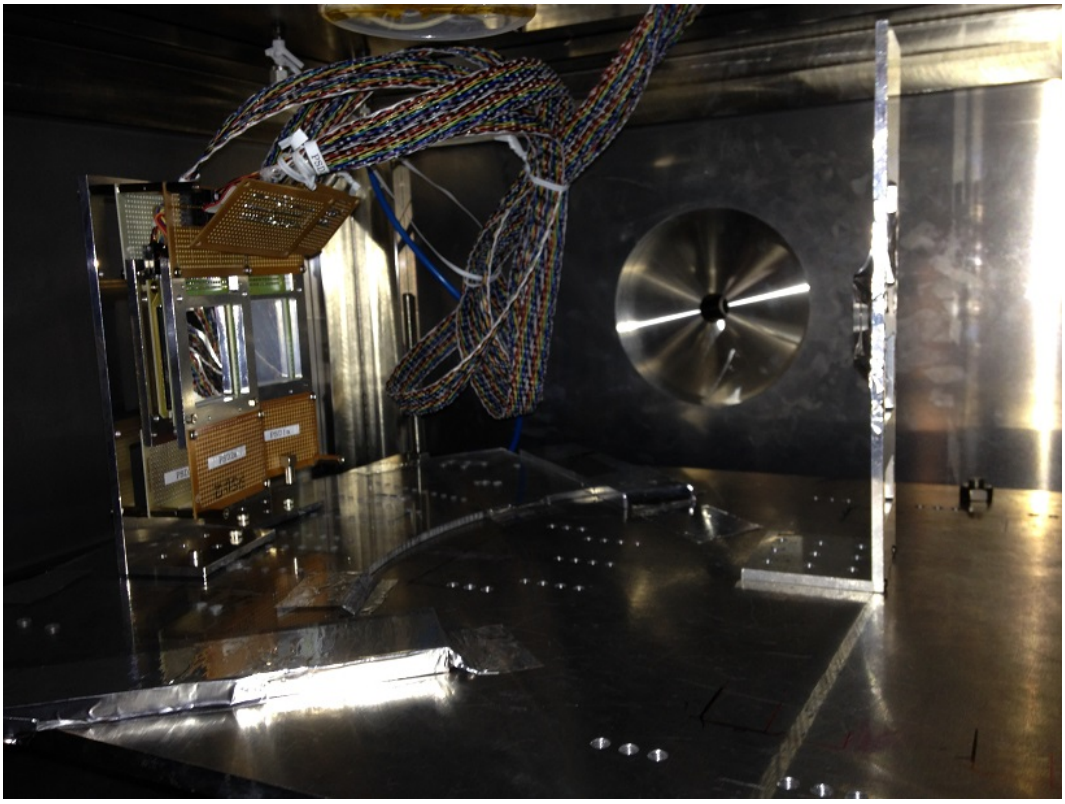

Figure 2.4: Picture of our setup. The telescopes were on the left side in this picture. The metal holder on the right side in this picture held an α source.

particle in this plot are explained in Subsection 3.4.

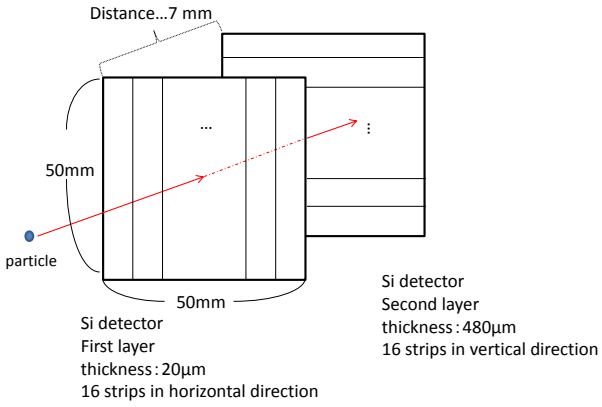

Figure 2.5: Overview of a telescope from front side. The thin Si detector was on the upstream. The thickness of the thin detector was 20 μm. There were 16 strips in the horizontal direction in the thin detector. The thick Si detector was on the downstream. The thickness of the thick detector was 480 μm. There were 16 strips in the vertical direction in the thick detector.

PSD

The measurement of the energy and the position was possible by PSD. Figure 2.7 is a picture of a PSD. 4 PSDs were used in this experiment. The PSDs have 50 x 50 mm^2 surface area. The surfaces of all the PSDs had 16 strips. 2 of them had strips in the horizontal direction (X direction), and 2 of them had 16 strips in the vertical direction (Y direction). Each strip works as an independent detector. If a particle hits a certain strip, the strip emit a signal and we are able to know which strip is fired.

2.5.3 PPAC principle

PPAC is often used at experiments with RI beams in order to measure the position and the counts of the beam. Figure 2.8 shows the construction of a delay-time PPAC. As Figure 2.8 shows, the PPAC main parts are composed of 2 cathodes and 1 anode. Gas such as C_3F_8 is filled in the PPAC. The voltage is applied between

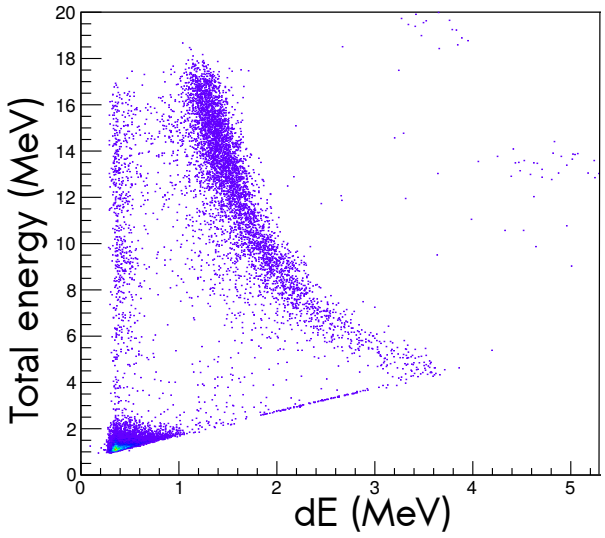

Figure 2.6: ΔE-E plot composed of events which were generated for two hours. A locus as a curve appears. The explanation about the selection of α is discussed in subsection. 3.4.

the anode and the cathodes. If radiations enter into the PPAC, some gas molecules are ionized, and the electrons drift to the anode, and the positive ions enter the cathodes. The electrons also cause the ionization effect at the gas, and secondary electrons are produced. The secondary electron also causes the ionization effect, and other secondary electrons are produced, i.e. the incident radiation causes electron avalanche. The positive ions enter the cathodes, and timing signals (T_{x1} and T_{x2}, or T_{y1} and T_{y2}) are obtained at the both ends of the cathodes. By taking difference of these two timing and multiplying a conversion factor (k_x/2 or k_y/2), the position (P_x, or P_y) of the radiation is measured. The equations for the conversion is as follows,

$$P_x = k_x/2\times(T_{x1} - T_{x2}) \tag{2.1}$$
$$P_y = k_y/2\times(T_{y1} - T_{y2}) \tag{2.2}$$

Table 2.2 shows the values of the factors to convert timing subtractions into the positions.

The Anode emits the timing signals of the beam hitting. We used these timing signals to make triggers.

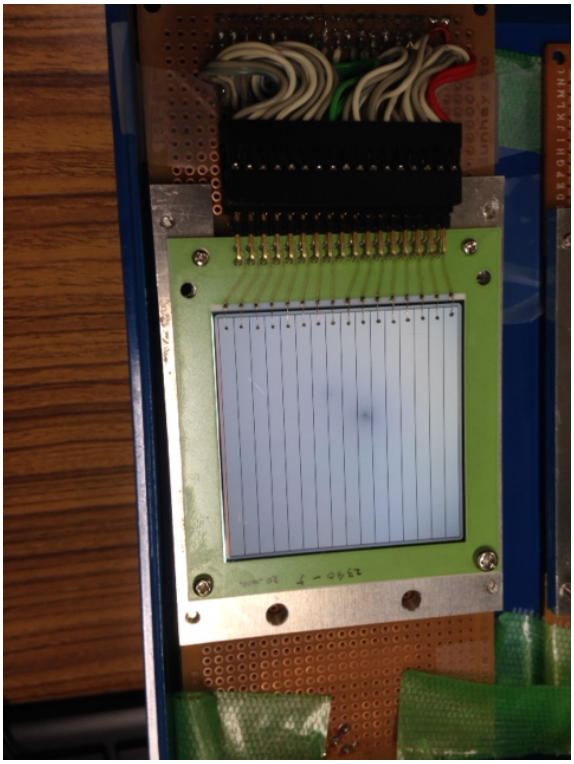

Figure 2.7: Picture of a horizontal-direction sensitive PSD. The surface had 16 strips in horizontal direction.

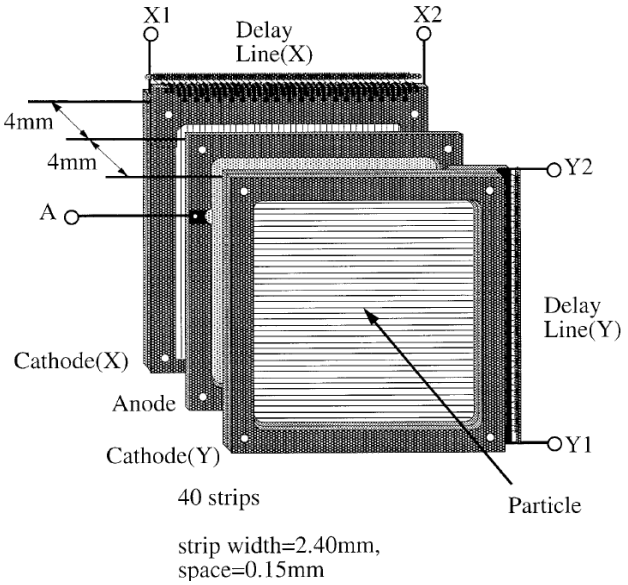

Figure 2.8: Diagram of cathodes and an anode in a PPAC.

	PPACa	PPACb
$k_x/2$ (mm/ns)	0.6205	0.6205
$k_y/2$ (mm/ns)	0.6165	0.6165

Table 2.2: Factors to convert timing subtractions into positions

2.6 Electronics

2.6.1 Overview

Figure 2.9 shows an overview of the electronics which were used in this experiment. Signals from the PSD1a passed through pre-amplifiers and were split into three paths. The first path was for the signals which passed through shaping amps and reached ADCs. The second path was for the signals which passed through fast amps and constant fraction discriminators (CFD), and reached TDCs. The third path was for the signals which passed through shaping amps which had low gains and reached ADCs. Signals from the PSD1b, the PSD2a and the PSD2b passed through pre-amplifiers and were split into two paths. For these signals, there were no path for signals passing through shaping amps which had low gains.

The purpose of the path for the signals passing through the shaping amps which had low gains from PSD1a was measuring the beam energy, in addition

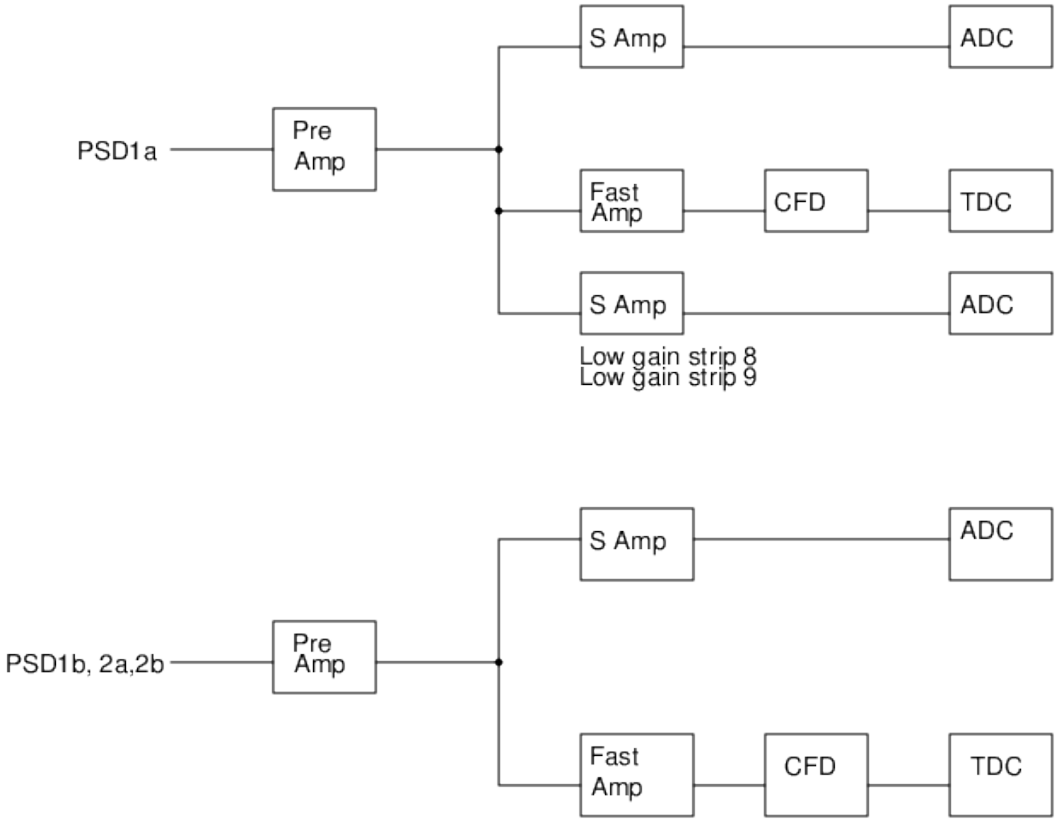

Figure 2.9: Diagram of electrics.

to the light particle energies. The beam energy was planned to be measured with the PSD1a and the PSD1b. The shaping amps which were in the first path had too high gains to measure the energy of the beam which hit the PSD1a. Therefore the third path in which the low-gain shaping amps was installed was added. The beam energy measurement is explained in Section. 3.3.

2.6.2 Trigger condition

The trigger condition used during this experiment was

$$Trigger \quad = \quad Beam/n + (\sum_i PSD_i) \times Beam \tag{2.3}$$

The trigger circuit is shown in Figure 2.10. The widths of the signals are shown in Figure 2.11.

The trigger *Beam* was created with,

$$Beam \quad = \quad (PPACb) \times \overline{pileup} \tag{2.4}$$

$$\tag{2.5}$$

There should be particles which pass through the PPACa, but did not hit the PPACb. Therefore the PPACb was used to create the triggers in order to discard events in which the ^{10}Be particle did not enter into the F3 chamber. Eliminating *pile-up* signals, signals from the PPACb reached the electronics within 500 ns after the last signal reached (at ② shown in Figure 2.10), was necessary, since the PPACs were not able to measure the positions of more than two particles at the same time. *n*=1000 was a factor to downscale the *Beam* signals in order to avoid the situation in which our DAQ was too busy to obtain the events in which ^{10}Be+α elastic resonant scattering occurred. $(\sum_i PSD_i)$, signals added all the signals from the PSDs were making triggers in coincidence with the *Beam* signals.

The trigger condition was designed in order to measure the excitation function. Counting the events in which the ^{10}Be particles entered into the reaction chamber and the events in which ^{10}Be+α resonant elastic scattering occurred were necessary (the details of calculating the excitation function is explained in Chapter. 3). The triggers of *Beam/n* were used to measure the number of the ^{10}Be particles which entered into the F3 chamber. The triggers of $(\sum_i PSD_i) \times Beam$ were used to count the events in which the ^{10}Be hit the PPAC and entered into the reaction chamber before the scattered α particle hit the PSDs.

Data taking was performed by BabarlDAQ [27] which is RTLinux-base CAMAC/VME data taking system. We used Anapaw [28] for the online analysis.

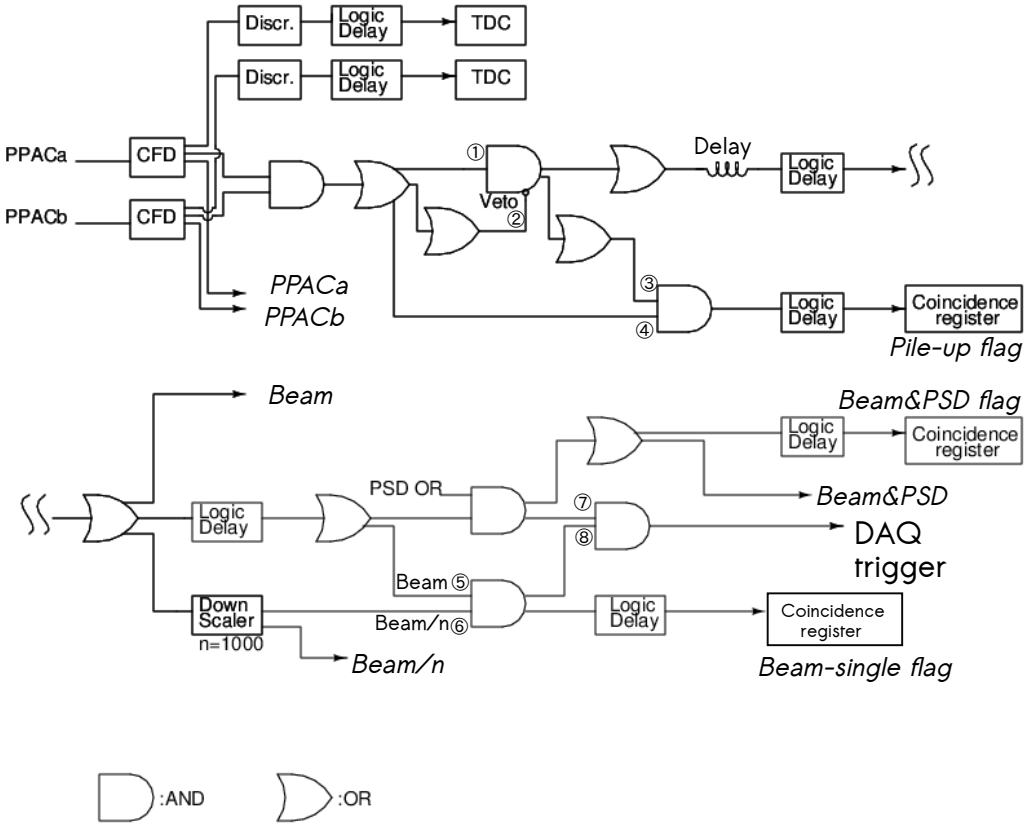

Figure 2.10: Diagram of trigger condition.

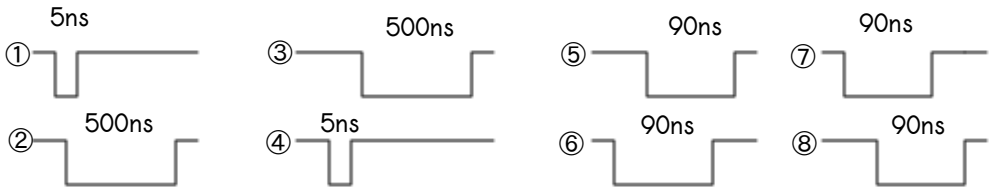

Figure 2.11: Width of signals.

2.7 Calibration

2.7.1 Calibration for each detector

We had two α sources that emitted 4.780, 5.480 and 5.795 MeV α particles and 3.148, 5.762 and 5.771 MeV α particles. The first layer detector was too thin for α particles which had an energy over 4.4 MeV to stop inside. If the particles do not stop inside the detectors, the particles do not lose their all energy. Hence we do not know how large the particles lose energy, and do not have the correspondence between MeV and channel.

In order to degrade these particles, we used 12 μm Al foil. We set the 12μm Al foil in front of the source which emitted 4.780, 5.480 and 5.795 MeV α particles so that the α particles passed through the foil and lost their energies sufficient to stop inside the thin detector. Table 2.3 shows calculated energies of the α particles. These α particles lost their energies sufficiently. Therefore they should stop inside the thin detectors.

Original α particles (MeV)	After 12μm Al foil from calculation (MeV)
4.780	1.872
5.480	2.988
5.795	3.397

Table 2.3: Energies of α particles which pass through a 12μm Al foil in calculation

The second-layer detectors were thick enough for the α particles from another source which emits 3.1462, 5.462 and 5.771 MeV particles to stop inside. Hence we obtained the calibration for those. We were able to calibrate the thick detectors in the method of setting the α source in front of the thick detector. In order to calibrate thin detectors, we firstly calibrated the thick detectors, measured the energies of the α particles which passed through the 12 μm Al foil with the thick detector, and used those energies for the thin detectors.

2.7.2 Result of calibration for each detector

The thick detectors were calibrated with the α from the source (shown in Figure 2.12). The energies of the α particles which passed through the 12 μm Al foil measured by the PSD1b are shown in Table 2.4 and by the PSD2b are shown in Table 2.5. The energies from the PSD2b were smaller than the energies from the PSD1b, since the PSD2a and PSD2b were angled against the Al foil, and the PSD1a and the PSD1b were installed in parallel against the foil. The thickness for the particle which hit the PSD2a and the PSD2b was longer than the thickness

for the particle which hit the PSD1a and the PSD1b. Therefore the energy losses of the particles to the PSD2a and the PSD2b were larger than the energy losses of the particles to the PSD1a and the PSD1b. The angles against the foil were almost same between the PSD1a and the PSD1b, and between the PSD2a and the PSD2b. Hence we used the energies shown in Table 2.4 for the PSD1a and the energies shown in Table 2.5.

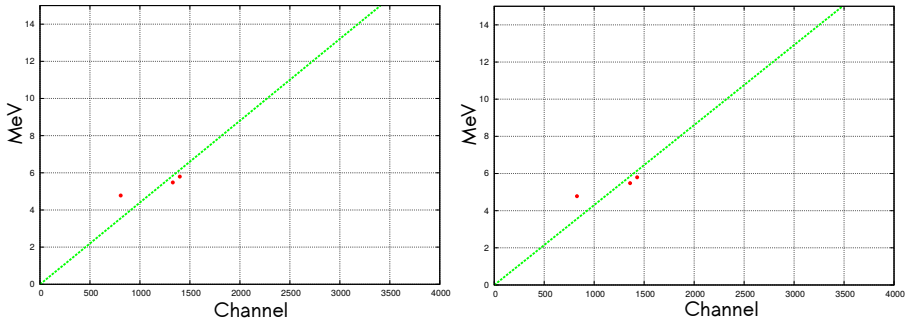

Figure 2.12: Left plot is the calibration for the PSD1b, and right plot is the calibration for the PSD2b. Red data points are derived from the α source. The data points are fitted with a linear function which is green dashed line. The data point of the lowest energy is the farthest from the dashed line. However in order to include the behavior of the detector in the wide energy range, this green line is used for calculation for energies.

Original α particles (MeV)	After 12μm Al foil (MeV)
4.780	2.57
5.480	3.55
5.795	3.94

Table 2.4: Energies of α particles which passed through the 12 μm Al foil. These energies were measured with the PSD1b which had been calibrated. The average of the energies measured with the all strips is shown.

The results of the calibration for the PSD1a and the PSD2a are shown in Figure 2.13. The non-foiled another source emitted 3.148 MeV α particles which stopped in the thin detectors were used for the calibration. Figure 2.14, Figure 2.15, Figure 2.16 and Figure 2.17 show the result of the calibration for all the strips (in this calibration run, the α source which emitted 3.148 MeV α particles was removed).

Original α particles (MeV)	After 12μm Al foil (MeV)
4.780	2.48
5.480	3.45
5.795	3.87

Table 2.5: Energies of α particles which passed through the 12 μm Al foil. These energies were measured with the PSD2b which had been calibrated. The average of the energies measured with the all strips is shown.

Statistics of the ninth strip of the PSD1a shown in Figure 2.14 was low. The reason could be that the value of the CFD threshold was not suitable. There was a slope in the line of the energies in the plot shown in Figure 2.16. This slope was derived from the extra foil thickness which was increased for the more angled strip. The first channel corresponded to the first strip in the detector, and the angle was larger than the sixteenth strip which corresponded to the sixteenth channel.

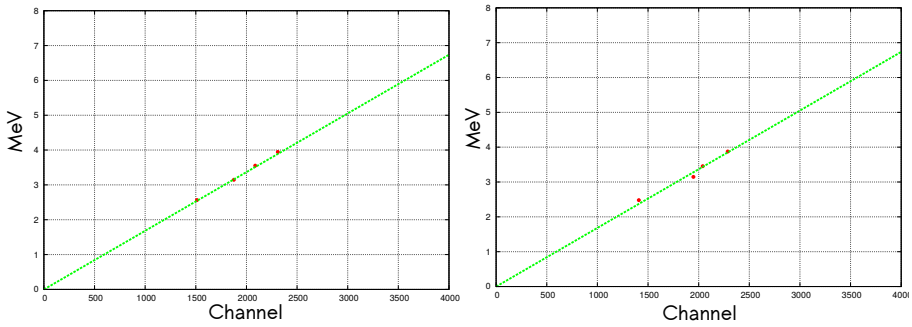

Figure 2.13: Left plot is the calibration for the PSD1a, and right plot is the calibration for the PSD2a. Red data points are derived from the α source. The data points are fitted with a linear function which is dashed green line.

The resolutions in the method of the calibration are shown in Table 2.6. The resolutions of the PSD1b and the PSD2b are derived from three data points from the α source without the Al foil. The resolutions of the PSD1a and the PSD2a are derived from one data points of 3.18 MeV α particle which did not pass through the Al foil.

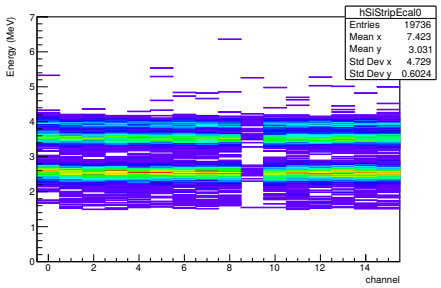

Figure 2.14: Calibration for all the strip in the PSD1a.

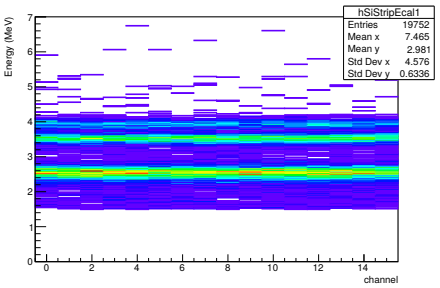

Figure 2.15: Calibration for all the strip in the PSD1b.

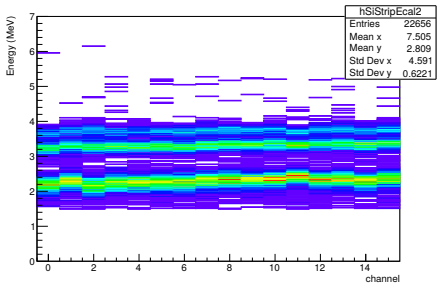

Figure 2.16: Calibration for all the strip in the PSD2a.

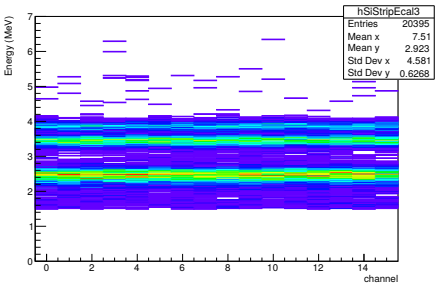

Figure 2.17: Calibration for all the strip in the PSD2b.

Detector	Resolution (keV)
PSD1a	74
PSD1b	33
PSD2a	57
PSD2b	25

Table 2.6: The resolutions determined by α energies without the foil. These resolutions were determined by taking the average of the standard deviation in the data points.

2.7.3 Correction of He gas and dead layer

Steps of correction

There were dead layers on the upstream side and the downstream side of each detector as shown in Figure 2.18. He gas was between the first detector and the second detector. The second thick detector was 7 mm distant from the first thin detector.

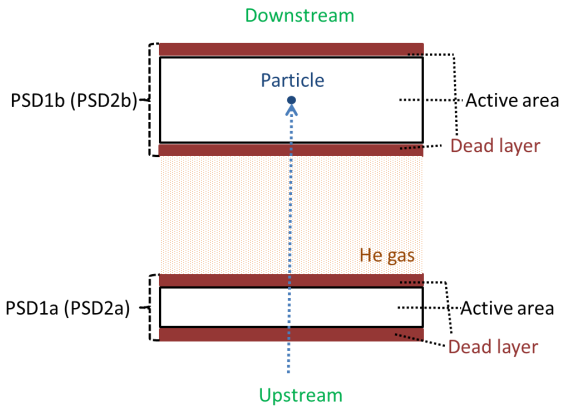

Figure 2.18: Top view of a telescope. There were dead layers on the upstream side and the downstream side of each detector. The reaction chamber was filled with 700 Torr He gas. Hence the He gas was between the first detector and the second detector. The distance from the first detector to the second detector was 7 mm.

The dead layers on the upstream side of the first detector and the second detector did not cause a big trouble since the channel corresponded to the original

energies of the α particles from the source even though the α particles passed through the dead layer. However the dead layer on the downstream side of the first detectors caused energy loss of particles which pierced the detector, and the energy loss was not able to be measured. The He gas also caused energy loss, and the energy loss was not measured. In order to measure the energy as close to the original energy as possible, correcting these extra energy loss in the dead layer and the He gas was necessary.

The steps for the correction were as follows.

- Obtaining the deposited energy in the second thick detector (E_{b}).
- By using the function fitted to the points calculated with the enewz, which is composed of codes made by Ziegler et al. [29] for calculation, reproducing the energy (E_{He}) which the particles had before those passed through the He gas from E_{b}.
- By using the function fitted to the points calculated with enewz, reproducing the energy (E_{dead}) which the particles had before those passed through the dead layer from E_{He}.
- Adding the deposited energy in the first thin detector to the E_{dead} and making the total energy (E_{total}).

Deposited energy in the thick detector versus energy loss in He gas

The energy loss in the He gas was calculated with enewz. Figure 2.19 shows the polynomial function (green dashed line) fitted to the points calculated with enewz. The polynomial function was used in order to modify the energy loss. The energy loss in the He gas was derived purely from this calculation.

2.7.4 Dead layer

In order to simulate the energy loss in the dead layer, determining the thickness of the dead layer was necessary. The thickness of the dead layer was determined together with the thickness of the window foil and the active area of the first thin detector. We measured the energy of α particles from the source and in α beam measured with the telescopes. The energies of the α from the source were 4.780, 5.480 and 5.795 MeV. The energies of the α beam were 11.0 and 15.0 MeV. The deposited energies in the first thin detector and the second thick detector were measured, and the extra energy losses were determined by subtracting the total deposited energies from the original energies. The thicknesses of the window, the active area and the dead layer were used as parameters in the least squared

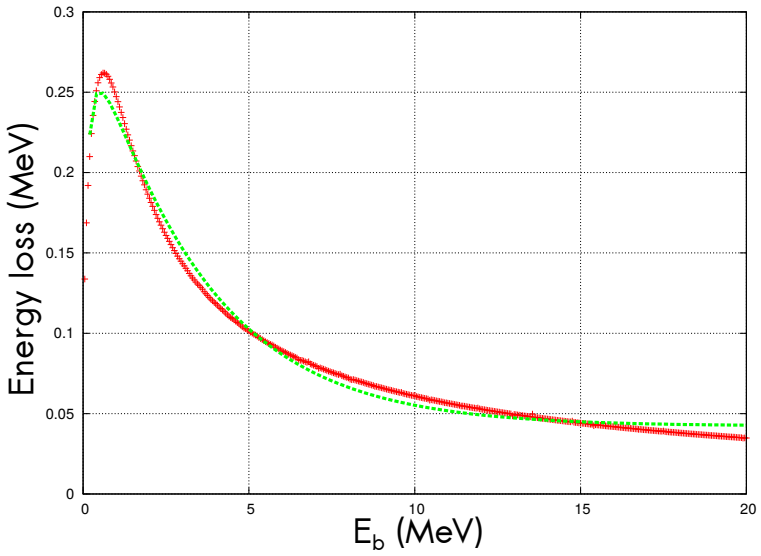

Figure 2.19: Energy loss in the He gas versus the deposited energy in the second thick detector. The red crosses are points calculated by enewz as energy loss in the He gas. The green dashed curve is fitted polynomial function.

method, and the thicknesses were determined as the parameters which can reproduce the energy measured in the experiment best. The thickness of the window was determined as 17.6 μm. The thickness of the active area was determined as 20.0 μm. The thickness of the dead layer on the downstream of the PSD1a was determined as 0.4 μm. After determining the thickness of the dead layer, we calculated the energy loss in the dead layer with enewz (shown in Figure 2.20). The green dashed line is a fitted polynomial function. This function was used in order to correct the energy.

Resolution as telescope

The thickness of the dead layer in the angled telescope was not determined. Hence only the resolution of the centered telescope was determined as 76 keV. The resolution was standard deviation which was derived from the α source and the α beam.

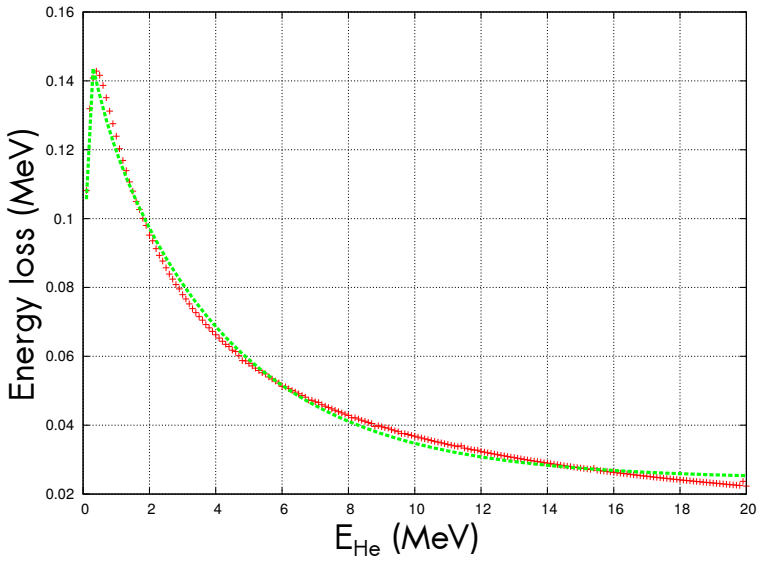

Figure 2.20: Energy loss in the dead layer versus E_{He}. The red crosses are points calculated by enewz as the energy losses in Si. The green dashed curve is the fitted polynomial function to the red points.

Chapter 3

Analysis

3.1 Determination of reaction points

In order to determine the parameters of the resonances of ^{14}C, a plot of cross section versus excitation energy $E_{\rm ex}$, excitation function is necessary. $E_{\rm ex}$ is calculated from $E_{\rm cm}$ with $E_{\rm ex}$ = $E_{\rm cm}$ + ^{10}Be+α *threshold* (12.01 MeV). Hence $E_{\rm cm}$ and cross section were required.

Cross section was calculated with,

$$\frac{d\sigma}{d\Omega_{\rm cm}} = \frac{Y_\alpha S(E_{\rm beam})}{I_{\rm beam} {\rm n} E_{\rm bin} \Delta\Omega_{\rm cm}} \frac{m_\alpha}{m_\alpha + m_{\rm Be}} \tag{3.1}$$

$$\begin{aligned}
Y_\alpha &= \text{Yield of } \alpha \text{ particles at each bin.} && (3.2)\\
S(E_{\rm beam}) &= \text{Stopping power of the He gas for the}^{10}\text{Be beam.} && (3.3)\\
\frac{m_\alpha}{m_\alpha + m_{\rm Be}} &= \text{factor to convert } S(E_{\rm beam}) \text{ into } S(E_{\rm cm}). && (3.4)\\
I_{\rm beam} &= \text{Number of the } ^{10}\text{Be beam ions injected.} && (3.5)\\
n &= \text{Number density of the } \alpha \text{ particle in the He gas.} && (3.6)\\
E_{\rm bin} &= \text{Energy bin size.} && (3.7)\\
\Delta\Omega_{\rm cm} &= \text{Solid angle in center of mass scale.} && (3.8)
\end{aligned}$$

Determining $\Delta\Omega_{\rm cm}$ required information of the position at which reactions occur, since $\Delta\Omega_{\rm cm}$ was calculated with,

$$\Delta\Omega_{\rm cm} = 4 \times \cos\theta_{\rm lab} \times \Delta\Omega_{\rm lab} \tag{3.9}$$

$\theta_{\rm lab}$, angle between the beam line and the direction in which a recoiled particle

flies, was geometrically detemined between the reaction point and the PSD positon a particle hits. Hence it was necessary to determine where the reaction occurs in order to calculate the cross section.

We can kinematically calculate $E_{\rm cm}$ from the energy of the beam ($\rm E_{beam}$) and the energy of the α ($\rm E_{\alpha}$) with,

$$E_{\rm cm} = E_{\rm beam}(\text{reaction point}) \times \frac{\rm m_{\alpha}}{\rm m_{\alpha} + m_{Be}} \tag{3.10}$$

$$E_{\rm cm} = E_{\alpha}(\text{reaction point}) \times \frac{\rm m_{\alpha} + m_{Be}}{4 m_{Be} \cos^2\theta_{\rm lab}} \tag{3.11}$$

The beam position was extrapolated with the PPACa and the PPACb. Therefore the reaction point can be expressed one-dimensionally such as distance z from the entrance window, since the beam trajectory was three-dimensionally traced. We used z_1 as the distance from the window for the beam. $E_{\rm cm}$ depended on z_1 as the beam energy decreased as the beam passing through the target. The beam energy at the z_1 was calculated by subtracting the energy loss from the beam energy just after the entrance window. Then $E_{\rm cm}$ also depended on $E_{\rm beam}$ (beam energy just after the entrance window). Hence the $E_{\rm cm}$ was calculated with,

$$E_{\rm cm} = f_1(E_{\rm beam}, z_1) \tag{3.12}$$

The position where α particle hit on the PSDs can be measured. The $\theta_{\rm lab}$ was a function of z and the detection position. The α energy at the reaction point was calculated with the energy of the α at the telescope ($E_{\rm det}$). Hence, $E_{\rm cm}$ was calculated with the recoiled α particle such as,

$$E_{\rm cm} = f_2(E_{\rm det}, \theta(z_2)) = f_2(E_{\rm det}, z_2) \tag{3.13}$$

(We used z_2 as the distance from the window to the position of the α.)

The scattering is elastic, and the energy conservation should be applied. Therefore an equation such as,

$$f_1(E_{\rm beam}, z_1) = f_2(E_{\rm det}, z_2) \tag{3.14}$$

should be satisfied. The distance from the window to the reaction point, $z_{\rm r}$ was determined as this z_1 (=z_2). The beam trajectory was known. Hence the reaction point was determined three dimensionally with this $z_{\rm r}$. Figure 3.1 shows the $f_1(E_{\rm beam}, z_1)$ and the $f_2(E_{\rm det}, z_2)$. The intersection of the $f_1(E_{\rm beam}, z_1)$ and

the $f_2(E_{\rm det}, z_2)$ was the $E_{\rm cm}$ and the $z_{\rm r}$. Figure 3.2 shows the overview of the determination of $E_{\rm cm}$ and $z_{\rm r}$.

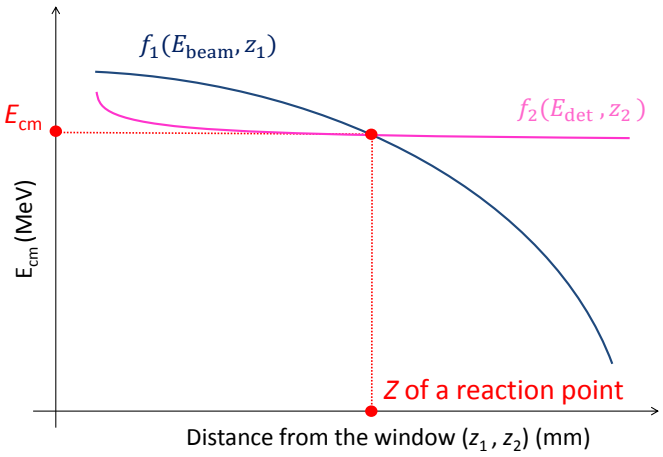

Figure 3.1: $E_{\rm cm}$ versus distance from the entrance window. Blue line is $E_{\rm cm}$ calculated from the beam energy. Pink line is $E_{\rm cm}$ calculated from the energy of α. The reaction is elastic. Therefore the $E_{\rm cm}$ from the beam energy was equal to the $E_{\rm cm}$ from the energy of α. The $E_{\rm cm}$ and the distance of the reaction point was determined as a red intersection.

The method how to obtain the $f_1(E_{\rm beam}, z_1)$ is explained in section 3.3. The details of $f_2(E_{\rm det}, z_2)$ are explained in Section 3.6.

3.2 Gate for ^{10}Be

In order to select the events of the scattered α particles, selecting only the events of the ^{10}Be particles with excluding contamination was neccesary.

3.2.1 Time of flight from F0 to F3

The RIKEN AVF cyclotron has 4 spiral sectors and 2 radiofrequency (RF) dee electrodes. We used the RF signals from the AVF cyclotron to analyze. Figure 3.3 shows the plot of the duration time ($\rm TOF_{RF}$) from the PPAC firing to the RF coming versus the particle position at the PPACa. The $\rm TOF_{RF}$ reflected the TOF from the F0 chamber to the F3 chamber, and the velocity basically depended on

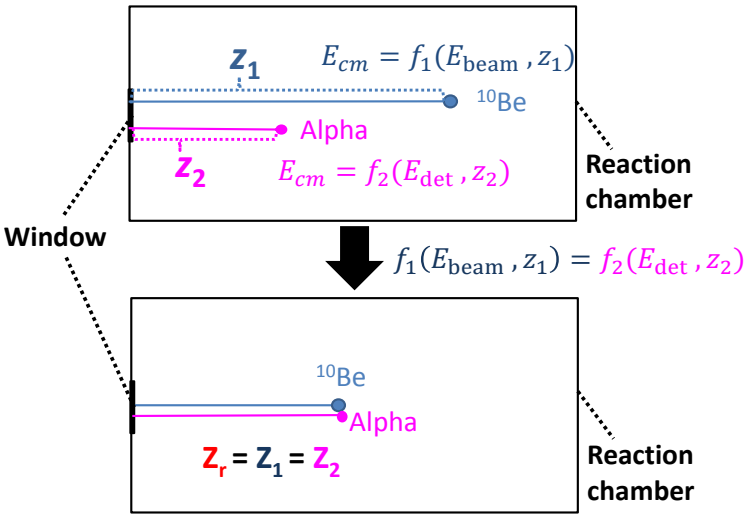

Figure 3.2: Overview of determining E_{cm} and the reaction point. z_1 was the distance from the entrance window to the position of the ^{10}Be. z_2 was the distance from the entrance window to the position of the α. The reaction was elastic. Hence when $f_1(E_{\mathrm{beam}}, z_1)$ was equal to $f_2(E_{\mathrm{det}}, z_2)$, E_{cm} was determined as this $f_1(E_{\mathrm{beam}}, z_1)$. One E_{cm} corresponded to only one reaction point. z_{r} was determined as z_1 (=z_2) which satisfied $f_1(E_{\mathrm{beam}}, z_1)$ = $f_2(E_{\mathrm{det}}, z_2)$.

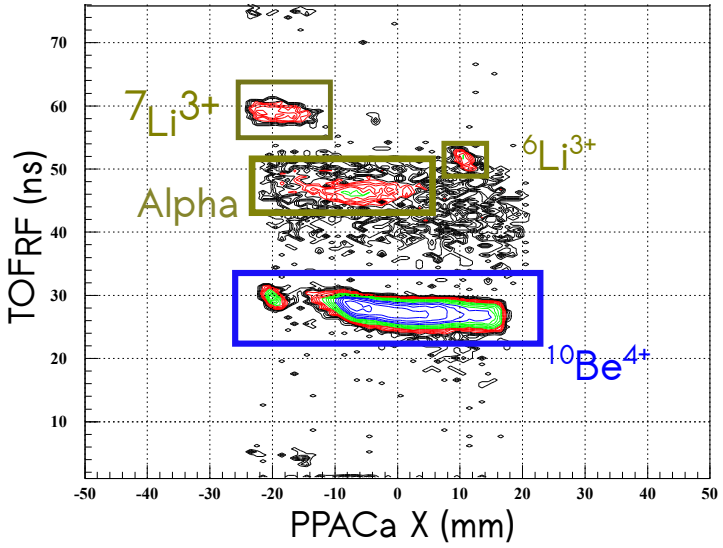

Figure 3.3: TOF_{RF} versus PPACa positions. This plot corresponds to a two-hour measurement. The events composed of ^{10}Be particles are in the blue frame.

the ion. Hence we used the TOF_{RF} to select only the ^{10}Be. PI for the ^{10}Be was performed at the F2 focal plane. With Wien filter, contamination was excluded and the position of the ^{10}Be at the PPACa was centered. Therefore we selected the locus which had the largest number of the particles and was centered at PPACa as seen in Figure 3.3, and used this range of TOF_{RF} as the gate for the ^{10}Be. As explained later, the structure of the excitation function was similar to the previous measurement of Freer et al. Hence this locus should be composed of the ^{10}Be.

3.2.2 Time of flight from PPACa to PPACb

The velocity dependance should be reflected to the duration time (TOF_{PPAC}) between PPACa and the PPACb. Figure 3.4 shows the plot of the TOF_{RF} and TOF_{PPAC}. The TOF_{RF} was determined with the PI seen in Figure 3.3, and the locus of ^{10}Be was chosen at the TOF_{RF} range. The blue frame shown in Figure 3.4 corresponds to the TOF_{PPAC} of the ^{10}Be.

3.2.3 Beam extrapolation

We defined $\mathrm{PPAC\,separation}$ as the distance from the PPACa to the PPACb. This value was fixed at the alignment as 299.5 mm. The extrapolation of the beam position was performed with the PPACa and the PPACb with,

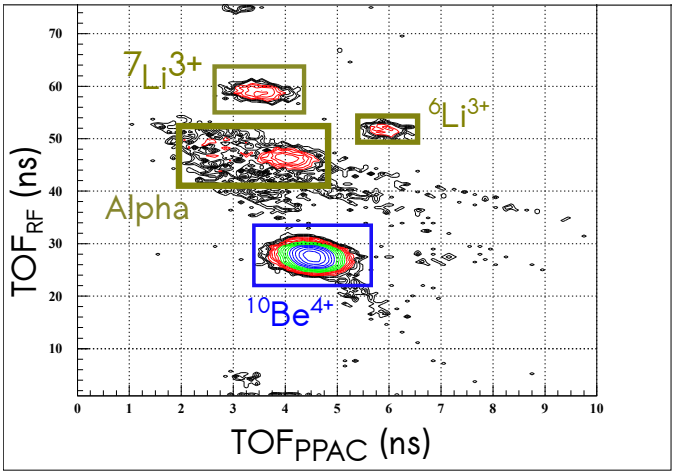

Figure 3.4: TOF_{RF} versus TOF_{PPAC}. This plot corresponds to a two-hour measurement. Events of ^{10}Be particles are in the blue frame.

$$X_z = X_a + \frac{z}{\text{PPAC separation}} \times (X_b - X_a) \tag{3.15}$$

$$Y_z = Y_a + \frac{z}{\text{PPAC separation}} \times (Y_b - Y_a) \tag{3.16}$$

The X_z was the x coordinate at z_1. The X_a was the x coordinate at the position of the PPACa. The X_b was the x coordinate at the position of PPACb. The beam centers at the PPACa and the PPACb in X_a, Y_a, X_b and Y_b were as follows.

$$X_a = -8.1\,(\text{mm}) \tag{3.17}$$

$$Y_a = -0.5\,(\text{mm}) \tag{3.18}$$

$$X_b = -2.8\,(\text{mm}) \tag{3.19}$$

$$Y_b = -0.1\,(\text{mm}) \tag{3.20}$$

3.2.4 Reaction chamber window

Even though we aligned the PPACa, the PPACb and F3 chamber, there was an offset of geometry. The center of the window on the front side of the reaction chamber was confirmed by plotting only the events in which the trigger was the PPACb $\times$ PSD. Only the particles which entered into the reaction chamber fired the PPACb $\times$ PSD trigger, and the particles which hit the wall outside the window

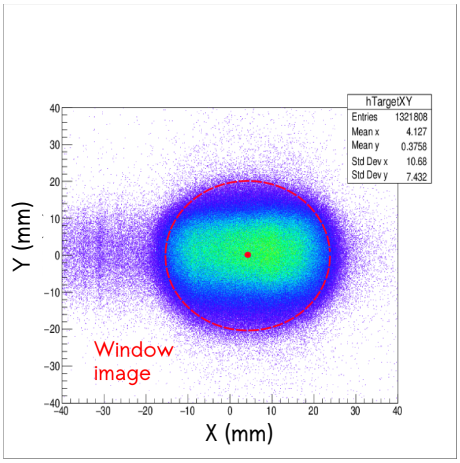

Figure 3.5: Extrapolated beam position on the entrance window of the F3 chamber. The center of the window was determined by taking triggers of the PPACb $\times$ PSD. The diameter was 4 cm. Red dash circle corresponds to the shape of the window.

did not fire the trigger. Hence, the plot of the extrapolated position of the beam on the window with the trigger of the PPACb $\times$ PSD corresponded to the shape of the window. The center of the window was determined as (-4.1, 0.4). A red dash circle which corresponded to to the window is drawn in Figure 3.5. The diameter of the window was 4 cm. We excluded the events in which particles had a distance more than 2 cm from the center.

3.3 Beam energy measurement

In order to determine the reaction point, we were required to know how the beam energy depended on z_1. The beam should hit the centered telescope. Therefore the centered telescope was used for the measurement for the energies. Several data points were required. Hence several measurements with changing the position of the centered telescope were required. However changing the position required venting the reaction chamber at each time, and venting the chamber takes long time. Hence we did not change the position of the telescope, but changed the pressure of the target gas several times. z_1 had the equivalent value at each pressure. We measured the beam energies at several pressures, and converted the pressure to the equivalent position in the gas target.

enewz requires inputting parameters such as pressure, temperature and so on. The parameters should have an offset against the ideal values to reproduce the

situation in the experiment. In this work, the temperature was fixed as 300 K. By fitting points calculated with enewz to the data points from this beam energy measurement, the pressure input was optimized to the experimental situation. Figure 3.6 shows the data points measured and fitted points calculated with enewz. The red points are from the measurement and the green curve is from calculation with enewz in which the optimized pressure (697.3 Torr) was input. This 697.3 Torr reproduced the situation the best. This optimized pressure was used every time when enewz calculation was performed.

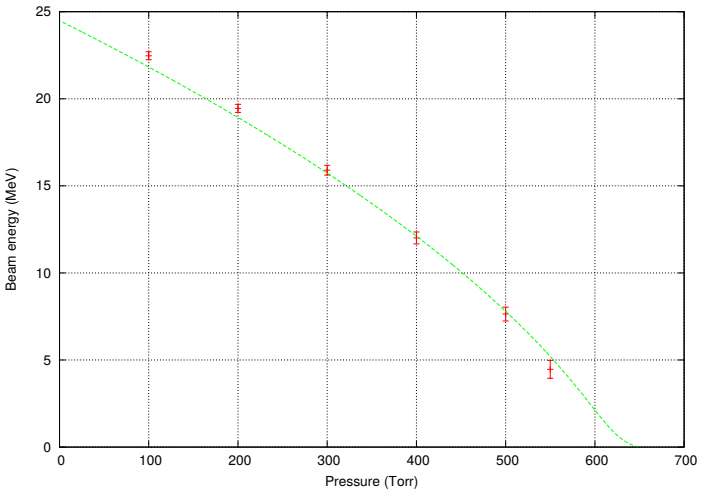

Figure 3.6: Beam energy versus pressure of the He gas. Red points are from measurement. The error is the standard deviation. Green dash line was calculated with enewz. Pressure offset of enewz was optimized to red data points. The offset was -2.7 Torr.

Figure 3.7 shows the relation between the beam energy and the distance after the converting the pressure into z_1. The data points were fitted to a certain polynomial function, $g(E_{\mathrm{beam}}, z_1)$. This function outputs the beam energy in laboratory system. Therefore converting to center-of-mass and constructing $f_1(E_{\mathrm{beam}}, z_1)$ were required and performed with,

$$g(E_{\mathrm{beam}}, z_1) \times \frac{m_\alpha}{m_\alpha + m_{\mathrm{Be}}} = f_1(E_{\mathrm{beam}}, z_1) \tag{3.21}$$

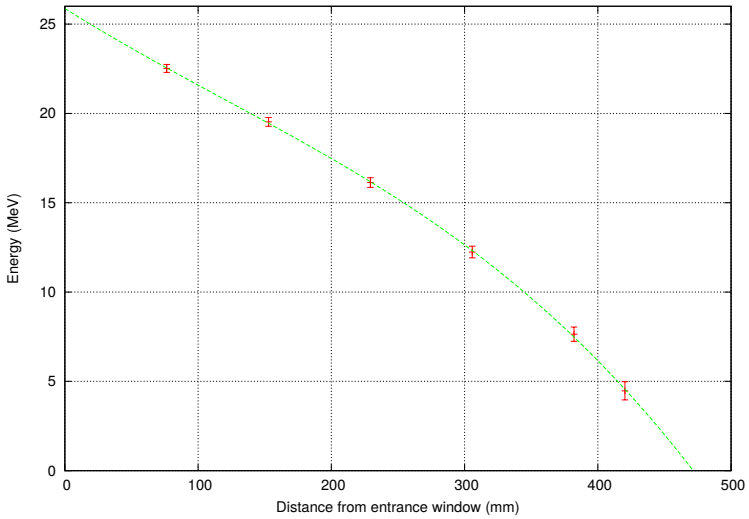

Figure 3.7: Beam energy versus distance from the entrance window to the position of the beam. Red points are from measurement. The error is the average of the standard deviation. Green dash line was calculated with enewz. The pressures were converted to the equivalent distances from the entrance window. Green dash line is polynomial fitted to the data points.

3.4 $\triangle E$-E α particle selection

Even though we selected the ^{10}Be beam precisely, some other contamination such as protons which were generated in the upstream entered into the reaction chamber. In addition protons were generated via a reaction of ^{10}Be(α, p) in the reaction chamber. Selecting α particles events with the ΔE-E plot was required. Figure 3.8 shows the ΔE-E plot after gating for the ^{10}Be. The thickness of the first detector was about 20 μm. The maximum α energy deposited in the first layer was calculated with enewz was about 4.4 MeV at this thickness of Si. The events with the highest α-particle energy corresponded to the scattering just after the entrance window. The beam energy just after the window was around 24.4 MeV (shown in Figure 3.6), and this energy corresponds to the maximum energy, around 17.1 MeV of the α. (The α energy is calculated with enewz.) By the deposited energy in the first detector and the maximum energy calculated by enewz, we chose the locus for the α in the ΔE-E plot. That is shown in Figure 3.8.

There was an overflow for the second-layer detector. Hence we did not obtain the data at pressure 0 Torr corresponding to the beam energy just after the window foil. Therefore there were two reproduced beam energies as at 0 Torr (shown in 3.6 and 3.7). The former energy was 24.4 MeV and the latter energy was 25.9 MeV. The former energy was calculated with the least squared method using the data points from changing the pressures and the beam energy calculated by the $B\rho$ (shown in Table 2.1). The latter energy was the value of the fitted polynomial function which is input $z_1 = 0$. The former energy was derived from the data points which inlcluded the beam energy measurement and the beam energy just before the window foil. The latter energy was derived from the data points which included only the beam energy measurement. Hence the former energy was considered reliable and used.

3.5 Scattered α

After selecting α events we distinguished scattered α particles from other α particles which were generated at the upstream in CRIB. These beam-like α particles reach the reaction chamber. In order to distinguish the scattered α, we used the duration time between the time when the beam particle hit the PPACb and the time when the α particle hit the second thick detector in the telescopes. Figure 3.9 shows the plot of the duration time versus the particle energy.

The primary beam came to CRIB periodically by around 70 ns. As Figure 3.3 shows, the beam-like α reached the reaction chamber before the ^{10}Be beam. Relatively after α by around 20 ns, the ^{10}Be beam reached the reaction chamber. Relatively after the ^{10}Be by around 50 ns, the beam-like α came to the reaction

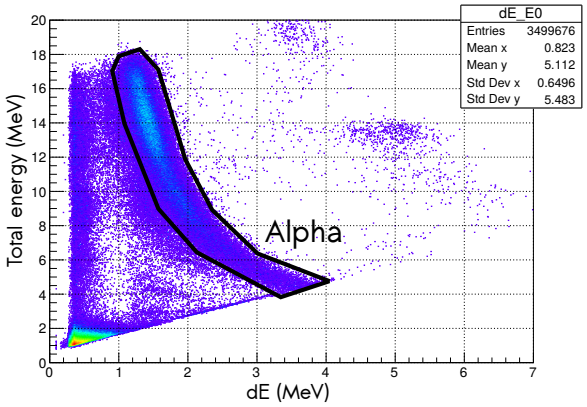

Figure 3.8: ΔE-E plot. This plot corresponds to a two-hours measurement. α locus was found.

chamber again since the period of the primary beam was around 70 ns.

In a typical scattering event, the ^{10}Be beam entered into the PPACb, reacted with the target α inside the reaction chamber, and the scattered α reached the second thick detector. Hence the duration time of the scattered α particle should be restricted within a certain time range.

There were some loci on the plot of the Figure 3.9. The scattered α particles created a locus on the plot. The other loci should be derived from the beam-like α. For example, the ^{10}Be fired the PPACb, may not react with the target α, and the beam-like α can reach the second thick detector in accidental coincidence. Some of the beam-like α particles followed the ^{10}Be beam with a delay of several tens of nano seconds. Then these events could creat a locus of which duration time was several nano seconds larger than the locus of the scattered α. We were required to distinguish the locus of the scattered α from the other loci.

We had the second telescope. The α particles which reached the second telescope should be mostly from the ^{10}Be+α scattering since the beam which includes contamination of α was not able to reach the second telescope due to the geometry. The α particles which reached the second telescope were derived only from the He gas in the reaction chamber. We compared the histogram from the centered telescope and the histogram from the angled telescope, and distinguished the scattered α particles locus.

Projected 2 histograms from Figure 3.9 are in Figure 3.10. The time range of the left histogram seen in Figure 3.10 was 260-305 ns. The time range of the right histogram seen in Figure 3.10 was 310-350 ns. Figure 3.12 is a projected histogram from Figure 3.11. The shape of peaks were obviously not similar be-

tween the two histogram in Figure. 3.10. Those were similar between the left histogram in Figure 3.10 and Figure 3.12. Therefore, not the time range of the right histogram in Figure 3.10, but the time range of the left histogram in Figure 3.10 should be selected. We compared each projected histograms from each time range of Figure 3.9 and Figure 3.12. We distinguished the time range of the scattered α particle as 260-305 ns.

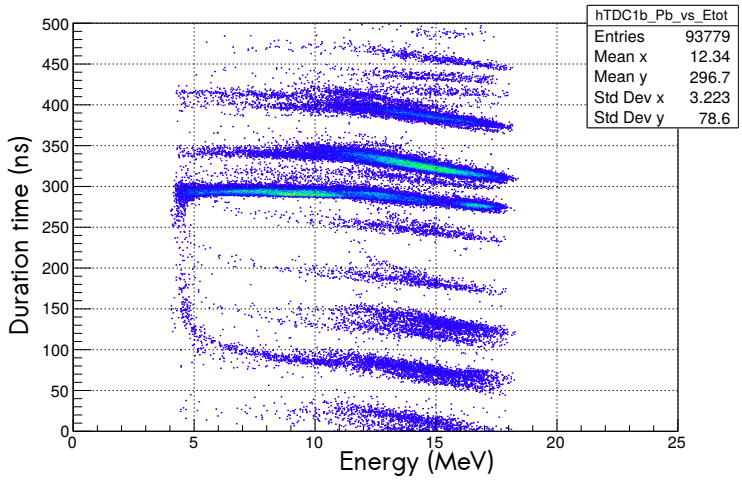

Figure 3.9: Duration time between PPAC1a and PSD1b versus energy. This plot includes events which were accumulated for 48 hours. Loci of this plot were from the scattered α and the beam-like α.

3.6 Calculation of $f_2(E_{\rm det}, z_2)$

After gating scattered α partiles, we calculated $f_2(E_\alpha, z_2)$ in order to determine the $E_{\rm cm}$ and the reaction point.

Figure 3.13 shows the schematic illustration of the kinematics reconstruction. The beam position was extrapolated by the PPACs. The α particle at a point was scattered on the beam trajectory, and reached the telescope.

We needed to search where the reaction was occured on the beam trajectory. We fixed z_2, and calculated x_2 and y_2, x coodinate and y coordinate of the beam trajectory with fixed z_2. We assumed the reaction was occured at the (x_2, y_2, z_2). We defined the energy of the α at the (x_2, y_2, z_2) as $E_{\rm at2}$. The hit position at the telescope was measured. Hence the scattering angle $\theta_{\rm lab}$ and the distance from the assumed reaction point to the hit position at the telescope, $l_{\rm a}$ were calculated by using (x_2, y_2, z_2).

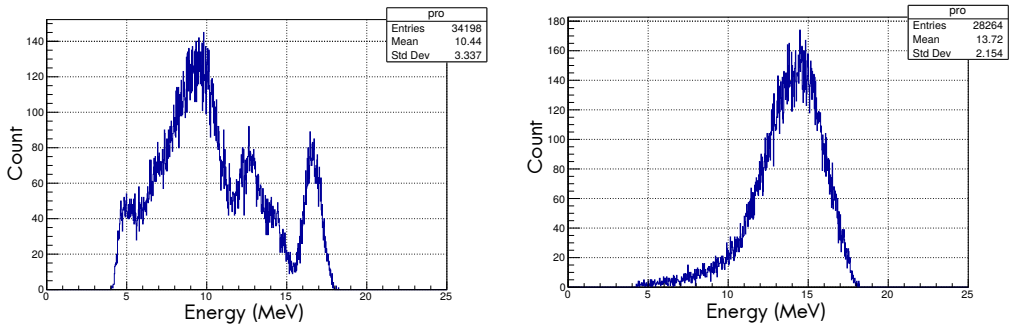

Figure 3.10: Count versus energy. Left histogram is projected with time range at 260-305 ns from Figure 3.9. Right histogram is projected with time range at 310-350 ns.

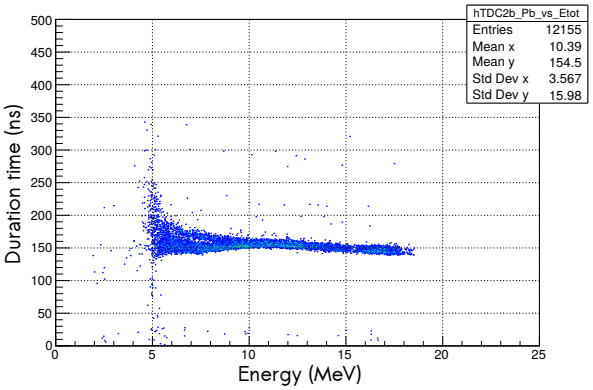

Figure 3.11: Duration time between PPAC2a and PSD2b versus Energy. This plot includes reaction events occured in 48 hours.

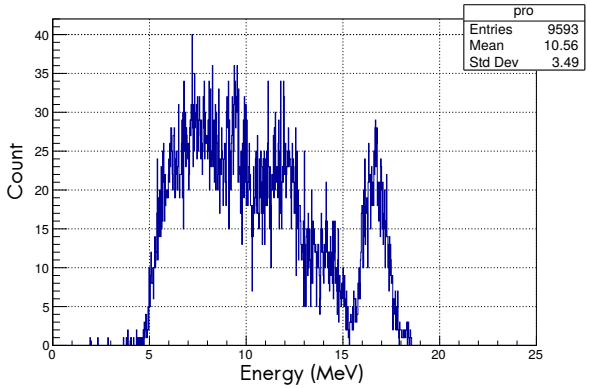

Figure 3.12: Count versus energy. Projection to energy axis from Figure 3.11.

If $E_{\rm det}$ and $l_{\rm a}$ were determined, we were able to calculate $E_{\rm at2}$, and then $E_{\rm cm}$. As α particle passed through the He gas by $l_{\rm a}$, it lost its energy in the He gas. By considering the energy loss, converting $E_{\rm det}$ into $E_{\rm at2}$ was required. The relation between the energy of the particle and a particle range is unique on a target. The pressure of the He gas was fixed as 700 Torr. By using this unique relation between the energy and the range, calculation of $E_{\rm at2}$ was performed.

Figure 3.14 shows the α energy-range curve in the 700 Torr He gas. The range corresponding to $E_{\rm at2}$ was longer than the range of the $E_{\rm det}$ by $l_{\rm a}$, since the α particle at the assumed reaction point did not pass through the He gas by $l_{\rm a}$. Hence the range corresponding to the $E_{\rm at2}$ was calculated as the range corresponding to the $E_{\rm det}$ added with $l_{\rm a}$.

We defined the range of the α particle at $E_{\rm det}$ as l. Figure 3.15 shows a inverse function against the function shown in Figure 3.14. By inputting $E_{\rm det}$ into the inverse function, we obtained l. We added this l to $l_{\rm a}$, inputted $l + l_{\rm a}$ into the function shown in Figure 3.14, and obtained $E_{\rm at2}$, as shown in Figure 3.16.

$E_{\rm cm}$ was calculated with $E_{\rm at2}$ and $\theta_{\rm lab}$ as shown in Equation 3.11. $E_{\rm at2}$ was calculated with $E_{\rm det}$ and z_2 as explained above. Hence $E_{\rm cm}$ depended on $E_{\rm det}$ and z_2. We used this $E_{\rm cm}$ as $f_2(E_{\rm det}, z_2)$.

3.7 Subtracting background

In Section 3.3, $f_1(E_{\rm beam}, z_1)$ was constructed. In Section 3.6, $f_2(E_{\rm det}, z_2)$ was constructed. $E_{\rm cm}$ and $z_{\rm r}$ were determined event by event with these functions. The histogram of the $E_{\rm cm}$ is shown in Figure 3.17.

Even though we created the gate for the events of ^{10}Be+α elastic resonant

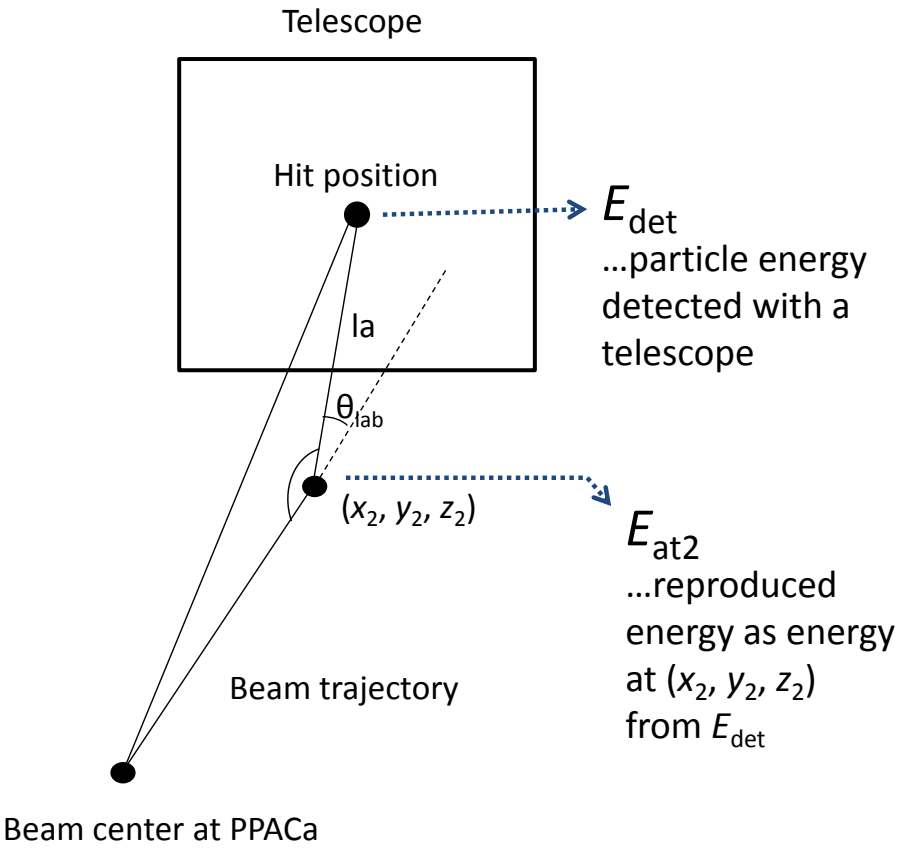

Figure 3.13: Diagram of ^{10}Be+α scattering. $E_{\rm det}$ is the detected energy of the particle at the telescope. The hit position on the telescope was also detected.

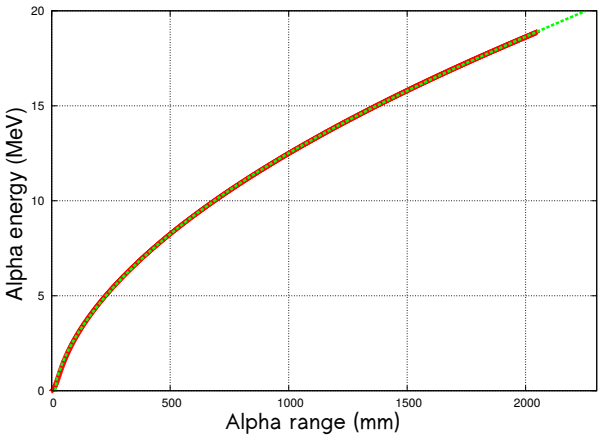

Figure 3.14: α energy-range curve in 700 Torr He gas. Red line was calculated with enewz. Green dashed line is a polynomial function fitted to the red line. The polynomial function was used for the calculation for the E_{at2}.

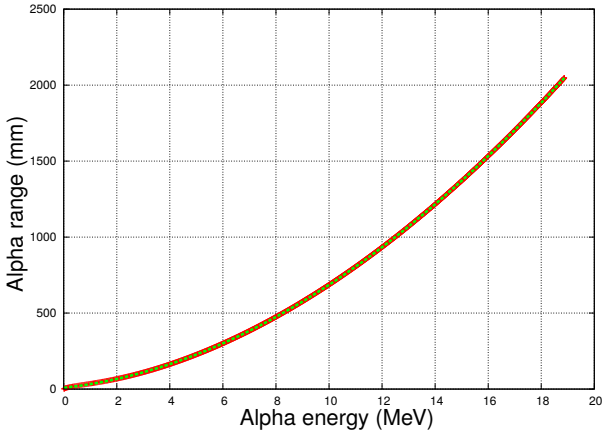

Figure 3.15: α range versus α energy on 700 Torr He gas. Red line waw calculated with enewz. Greed dashed line was a polynomial function fitted to the red points. The polynomial was used for the calculation of the l, the range corresponding to the E_{det}.

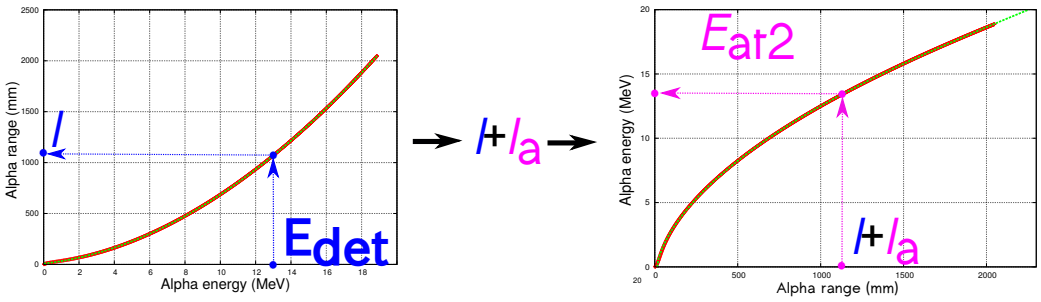

Figure 3.16: Procedure for calcuating the E_{at2}. Firstly calculating the l with the E_{det}. Secondary adding the l_{a} to the l. Thirdly inputting the $l+l_{\mathrm{a}}$ into the function fitted to the energy-range curve, and obtaining the E_{at2}.

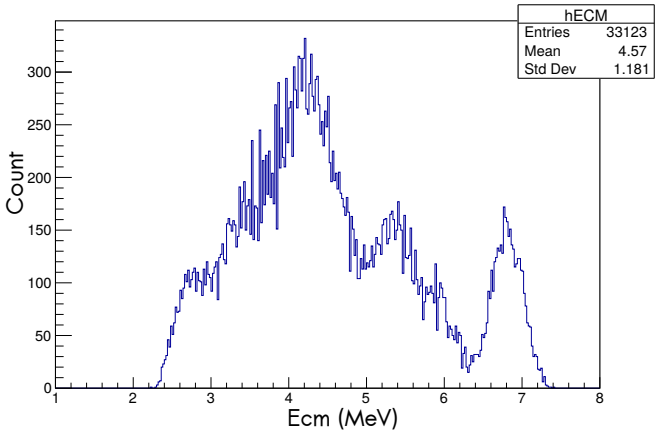

Figure 3.17: Count versus center-of-mass energy before subtracting background.

scattering and applied the gate for event selection, events from particles of contamination still remained. We applied the gate for the α. Hence the beam-like α should be contamination of the gated events. In order to measure the background, we used Ar gas. The pressure was fixed so that the thickness of the Ar gas was equivalent to the thickness of the 700 Torr He gas. We determined the equivalent pressure of Ar gas to the 700 Torr He gas during this experiment. Table 3.1 shows the relation of the beam energy, the Ar gas pressure and the He gas pressure measured during the experiment.

Beam energy (MeV)	Ar pressure (Torr)	He pressure (Torr)
5.9	90	
4.0		550
3.3	100	
(0)	Determined as 123.8	700

Table 3.1: Relation between beam energy and pressure of gas.

We assumed the linearlity on the relation between the beam energy and the gas pressure. From the 5.9 MeV, the 90 Torr, 3.3 MeV and the 100 Torr, we determined the Ar gas pressure corresponding to the 550 Torr He gas was 97.3 Torr. The ratio of $700(\mathrm{Torr})/550(\mathrm{Torr})$ at the He gas pressure was multiplied to 97.3 Torr Ar, and the equivalent pressure to the 700 Torr He gas was calculated as 123.8 Torr for Ar gas. To measure the background, the 123.8 Torr Ar gas was used.

Figure 3.18 shows the histogram from the data accumulated during the all background runs. The background is proportional against the number of the beam particles. Hence we needed to normalize the number of the ^{10}Be in the Ar gas run into the number of those in the He gas run in order to subtract the background.

The PPACs measured the count of particles reached the reaction chamber. The number of the events which were triggered by only the signals from the PPACs was downscaled by 1000 as explained in Subsection 2.6.2. Figure 3.19 shows the downscaled number of the ^{10}Be particles which was counted in the He gas runs as entries. The loci mostly consisted of the events of the ^{10}Be. Figure 3.20 shows the downscaled number of the ^{10}Be particles which are gated in the Ar gas runs same as in the He gas runs. The number of the entries from the He gas runs was 2546415, and that from the Ar gas runs was 1142631, then we multiplied $2546415/1142631 = 2.228554$ to the count in the histogram shown in Figure 3.18 and subtract it from the histogram shown in Figure 3.17. The histogram after subtracting the background is shown in Figure 3.21.

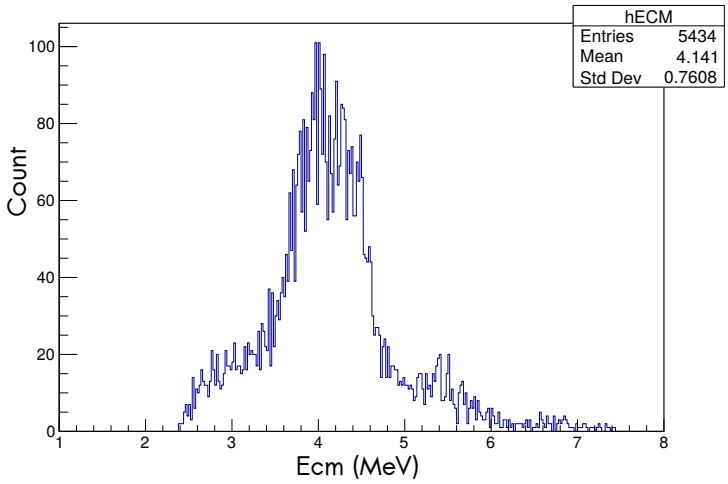

Figure 3.18: Count of background versus center-of-mass energy.

3.7.1 Stopping power

The stopping power is calculated as the energy loss of the ^{10}Be beam per 1 mm in the He gas. In the case of the thick target method, the thickness of the target changes depending on the beam energy at each energy bin. The high-energy beam just after the window loses lower energy at a certain fixed distance. Hence the path corresponding to the fixed energy bin is extended and vice versa. The length of the target which the beam passed through at each energy bin was calculated with,

$$\frac{S(E_{\mathrm{beam}})}{\Delta E} \times \frac{m_\alpha}{m_\alpha + m_{\mathrm{Be}}} \tag{3.22}$$

The stopping power was calculated with enewz (shown in Figure 3.22). The calculated points were fitted with polynomial functions for separated energy regions (shown in Figure 3.23), and we used the polynomial functions to calculate the cross section.

3.7.2 Number of ^{10}Be

The downscaled number of the ^{10}Be particles which entered into the reaction chamber with considered about the dead time of our DAQ is shown in Figure 3.19. The down scale factor was 1000. Hence the actual number of the ^{10}Be was 2546415×1000.

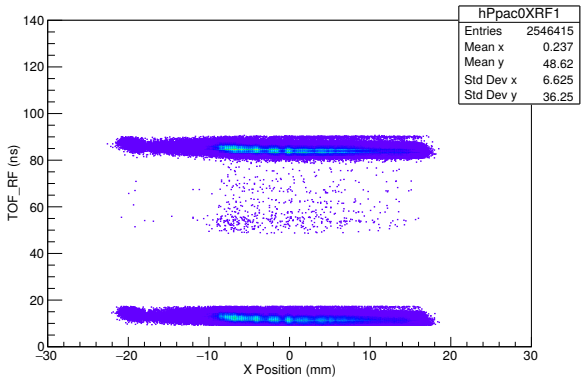

Figure 3.19: TOF_{RF} versus PPACa position in He gas runs. The selected time range is different from the Figure 3.3. The RF signals were separated into 2 paths in our circuit, and RF signals in one path of them were delayed. The RF signals used in Figure 3.3 were in the different path from the path for the RF signals used in this plot. Therefore the selected time range is different. The number of the time ranges of the gate for the ^{10}Be particles were three. The time ranges for the RF signals corresponding to the events shown in this plot were 10-19 ns and 80-90 ns. The time tange for the events in Figure 3.3 was 30-40 ns. These gates were performed as OR. There are events at 50-80 ns in this plot though the ranges of the gate were 10-19 ns or 80-90 ns. The reason could be the signals which became events in Figure 3.3 were delayed inaccurately in the path for this plot, and created events at 50-80 ns. These events were also counted as the number of the ^{10}Be particles. The count should be correct as the number of the ^{10}Be even though the events were at the time range which was not for the gate, since the events were created with only the triggers and the RF signals, and the time range itself did not relate with the number of the events.

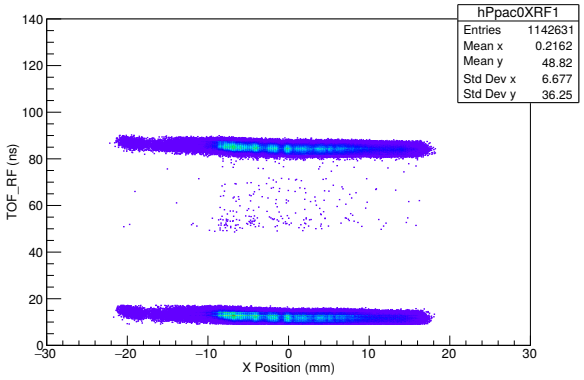

Figure 3.20: $\mathrm{TOF_{RF}}$ versus PPACa position in Ar gas runs. The reason why the time range is different from the time range in Figure 3.3 is same with Figure 3.19

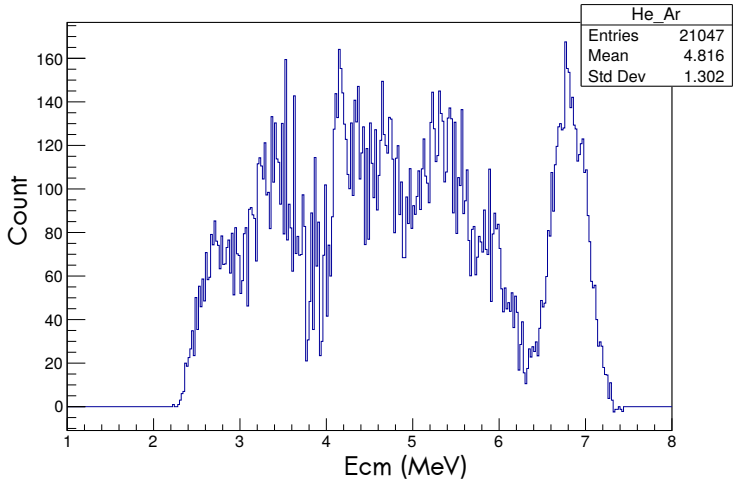

Figure 3.21: Count versus center-of-mass energy after subtracting background.

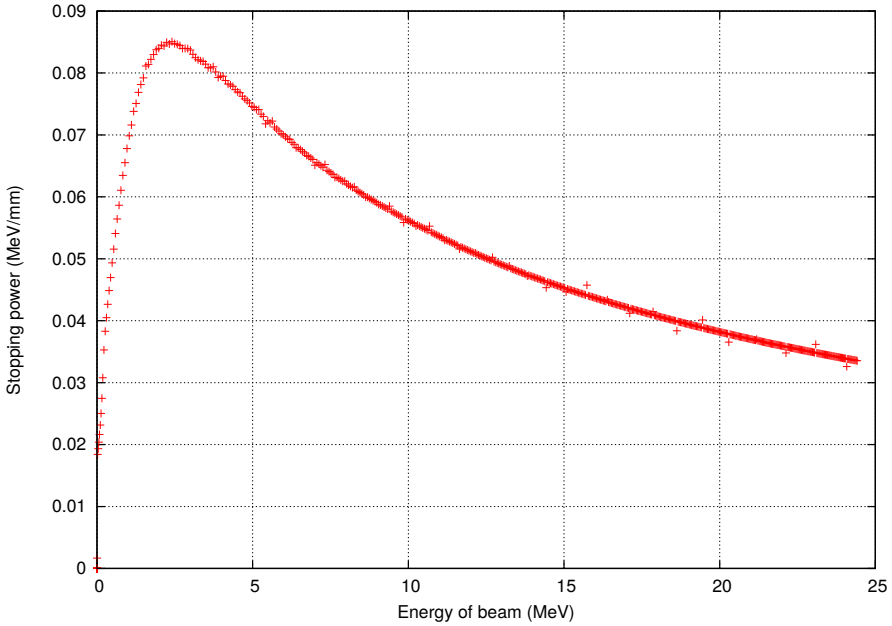

Figure 3.22: Stopping power, energy loss of beam per 1 mm in the He gas, versus energy of the beam. The red crosses were calculated with enewz.

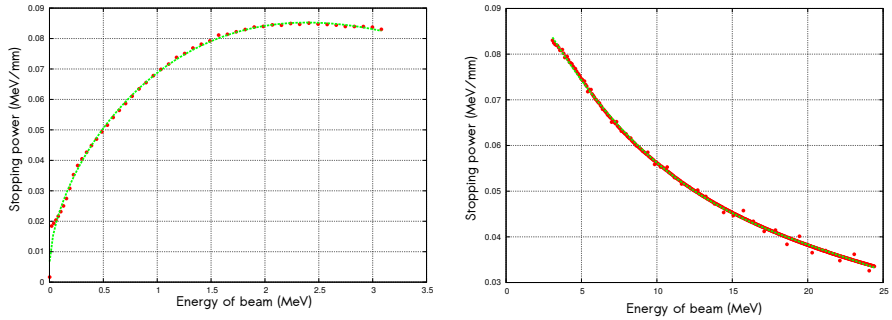

Figure 3.23: Stopping power versus energy of the beam same as Figure 3.22. The energy range of the left plot is 0-3.2 MeV, and the right is 3.2-24.4 MeV. The red points were calculated with enewz. The dashed green line were fitted with the red points.

3.7.3 Number density

The mass density of the target helium gas was calculated with LISE++ [30], as 1.5328×10^{-4} g/cm^3 at 700 Torr and 293.15 K.

The unit g/cm^3 was converted into /mm^3 (number density), using Molecular weight and Avogadoro's number relation. Helium atoms of 6.0221×10^{23} particles (Avogadoro's number) weigh 4.0026g. Then the number of the particles per 1 g was calculated as $6.0221\times10^{23}/4.0026\mathrm{g} = 1.5045\times10^{23}$ /g.

Then the number density per 1g becomes

$$\frac{\mathrm{g}}{\mathrm{cm}^3} = \frac{\mathrm{g}}{10^3\mathrm{mm}^3} = \frac{1.5055\times10^{23}}{10^3\mathrm{mm}^3} = 1.5055\times10^{20}/\mathrm{mm}^3$$

In the present target, the number density was

$$\begin{aligned} 1.5328\times10^{-4}\frac{\mathrm{g}}{\mathrm{cm}^3} &= 1.5328\times10^{-4}\times1.5055\times10^{20}/\mathrm{mm}^3 \\ &= 2.3076\times10^{16}/\mathrm{mm}^3 \end{aligned}$$

3.7.4 Solid angle

We converted the number of the yielded α at each energy bin into the cross section. In order to convert, we calculated the solid angle at each energy bin. $\Delta\Omega_{\mathrm{lab}}$, the solid angle in laboratory system was calculated with,

$$\begin{aligned} \Delta\Omega_{\mathrm{lab}} &= \frac{S^2}{l_a^2} \\ S &= \text{Surface area of telescope} \\ l_{\mathrm{a}} &= \text{Distance from reaction point to telescope} \end{aligned}$$

We determined the value at each energy bin as follows.

- After determining the reaction point, calculating the $\Delta\Omega_{\mathrm{lab}}$ event by event. Obtaining the data point of the E_{cm} and the solid angle.
- Plotting the solid angle versus the E_{cm}.
- Obtaining the average of $\Delta\Omega_{\mathrm{lab}}$ at some $\mathrm{E_{cm}}$ from the plot. Gaining the data points of the average $\Delta\Omega_{\mathrm{lab}}$ and $\mathrm{E_{cm}}$.
- Fitting a polynomial function to the data points, and obtaining the solid angle at a certain $\mathrm{E_{cm}}$.

The Figure 3.24 shows the relation between the $E_{\rm cm}$ and the $\Delta\Omega_{\rm lab}$ determined event by event.

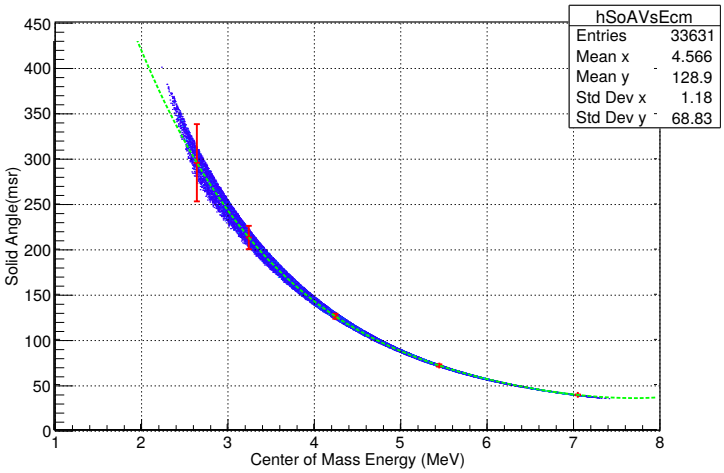

Figure 3.24: Solid angle versus $E_{\rm cm}$. Blue points are the solid angle determined event by event. Red points are average solid angles at each energy. The errors are standard deviation. A green dashed line is polynomial function fitted to the red points. The polynomial function was used to calculate the cross section.

From the plot of Figure 3.24, we constructed function to obtain the $\Delta\Omega_{\rm lab}$ from $E_{\rm cm}$. We used that function to calculate the cross section.

3.7.5 Conversion into center-of-mass system

The cross section calculated with $\Delta\Omega_{\rm lab}$ is in laboratory system. The excitation function should be expressed in center-of-mass system for the purpose of comparing excitation functions with previous measurements. In order to convert $\mathrm{d}\sigma/\mathrm{d}\Omega_{\rm lab}$, cross section in laboratory system, into $\mathrm{d}\sigma/\mathrm{d}\Omega_{\rm cm}$, cross section in canter-of-mass system, we used equations as follows.

$$\theta_{\rm cm} = \pi - 2\theta_{\rm lab} \tag{3.23}$$
$$d\Omega_{\rm lab} = d\phi_{\rm lab}\sin\theta_{\rm lab}d\theta_{\rm lab} \tag{3.24}$$
$$d\Omega_{\rm cm} = d\phi_{\rm cm}\sin\theta_{\rm cm}d\theta_{\rm cm} \tag{3.25}$$

$$\frac{d\sigma}{d\Omega_{\rm cm}} = \frac{d\Omega_{\rm lab}}{d\Omega_{\rm cm}}\frac{d\sigma}{d\Omega_{\rm lab}} = \frac{1}{4\cos\theta_{\rm lab}}\frac{d\sigma}{d\Omega_{\rm lab}} \tag{3.26}$$

3.7.6 Energy bin size

The energy resolution of the telescope was around 76 keV. There were other factors which should have caused the energy broading to be wider such as the energy broading of the beam which was generated at the F0 gas cell and entered into the F3 chamber, the window foil, the He gas and the histogram included wide range angles. The discussion about how large the energy broading should be performed, and to determine the bin size is necessary. However in order to interpret the feature of the excitation function roughly, the bin size was fixed as 100 keV in laboratory system. The 100 keV in the energy of the α particle in laboratory system corresponds to around 35 keV of $E_{\rm cm}$.

3.7.7 Excitation function

By using the factors explained above, the count of the α at each energy bin was converted into the cross section, and the excitation function was obtained as shown in Figure 3.25.

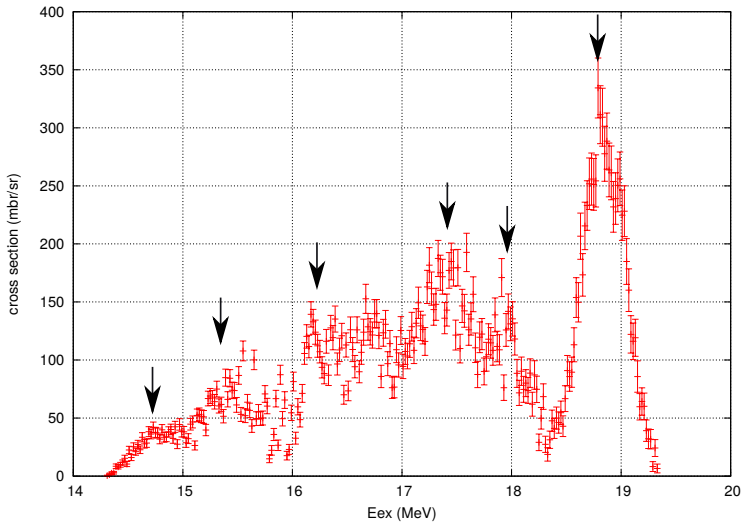

Figure 3.25: Cross section versus excitation energy from this experiment. Errors are in the standard deviation. Candidates of the resonances are pointed with black arrows. Angular region was 0-15.2 degrees in laboratory system. The average scattering angle was 8.1 degree in laboratory system.

From Figure 3.25, the peaks near 14.8, 15.3, 16.1, 17.3, 17.8 and 18.8 MeV could be interpreted as resonances, and the widths were determined roughly (shown

in Table 3.2).

E_{ex} (MeV)	Γ (keV)
14.8	200-300
15.3	400
16.1	
17.3	500
17.8	400-500
18.8	500-600

Table 3.2: Peaks which could be interpreted as resonances. The width, FWHM, was roughly determined by seeing the plot shown in Figure 3.25. The width of the peak at 16.1 MeV was not determined because of the shape.

Chapter 4

Discussion

4.1 Comparing with previous measurements

Haigh et al. [20] observed resonances in ^{14}C via ^{12}C(^{16}O,^{14}O)^{14}C* reaction, and determined the energies of levels shown in Table 4.1 and Figure 4.1. Freer et al. [21] performed an experiment of ^{10}Be+α resonant elastic scattering, and determined the parameters of the resonances at 16.5-22 MeV shown in Table 4.2 and Figure 4.2. Each of the resonance at 16.72, 17.5 and 18.6 MeV in the excitation function of Haigh et al. could correspond to the resonance at 17.32, 17.95 and 18.6 MeV in the excitation function of Freer et al. The reason why the energies of the resonances were different could be that the resonances correspond to other levels because of the different reactions.

E_{ex} (MeV)	J^{π}
12.96	(0^{-},2^{-},3^{-})
14.1	
14.87	(5^{-})
15.75	
16.72	
17.5	
18.6	(2^{-},4^{-},6^{-})

Table 4.1: Resonances possibly having a large α width observed in the experiment of Haigh et al. The reaction was 2n-transfer,^{12}C(^{16}O,^{14}O)^{14}C*.

E_{ex} (MeV)	J^{π}	Γ (keV)
17.32	3^{-}	(450, 590)
(17.95, 17.99)	(2^{+})	(420, 760)
(18.22)	(4^{+})	(200)
18.82	5^{-}	(500, 590)
19.65	5^{-}	(100, 140)
20.80	6^{+}	300

Table 4.2: Level, spin parity and α width determined in the experiment of Freer et al. The reaction was ^{10}Be+α resonant elastic scattering.

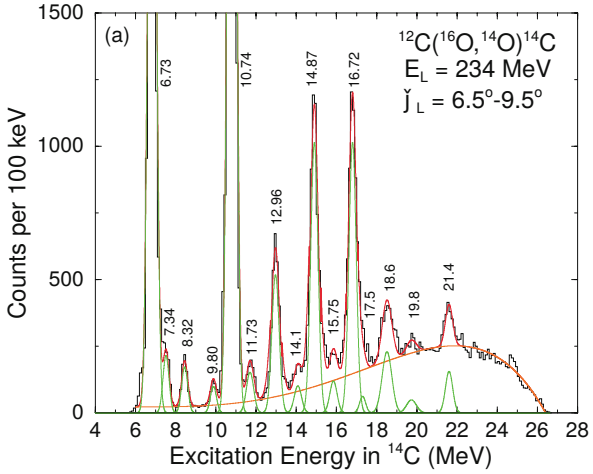

Figure 4.1: Measured resonances by Haigh et al. [20].

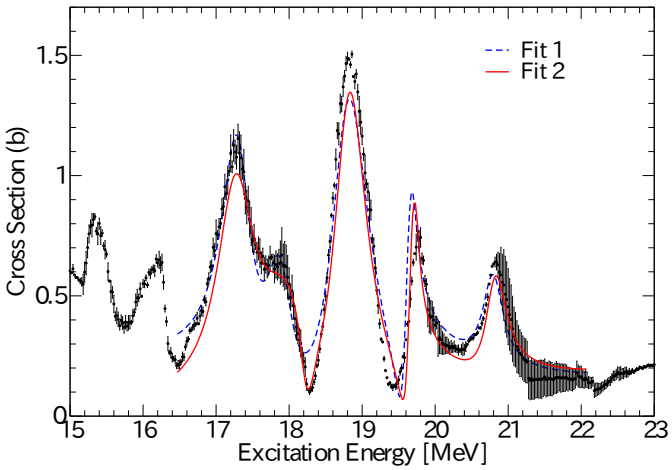

Figure 4.2: Excitation function by Freer et al. [21]. Black points are from measurement. Red line and blue dash line are fitted function by R-matrix calculation.

4.1.1 Comparing Energies of levels

There is a possibility that 14.87, 15.75, 16.72, 17.5 and 18.6 MeV resonances determined by Haigh et al. correspond to the 14.8, 15.3, 17.3, 17.8 and 18.8 MeV peaks we observed as Figure 4.3. The energies of resonances at 15.75, 16.72 and 17.5 MeV in the excitation function of Haigh et al. were unacceptably different from the energies of resonances at 15.3, 17.3 and 17.8 MeV in our excitation function. The reactions between Haigh et al. and us were different. Therefore the levels could be different each other. The resonances at 17.32, 17.95 (or 17.99) and 18.82 MeV by Freer et al. should correspond to the energies of the peaks at 17.3, 17.8 and 18.8 MeV in the present work as in Figure 4.4.

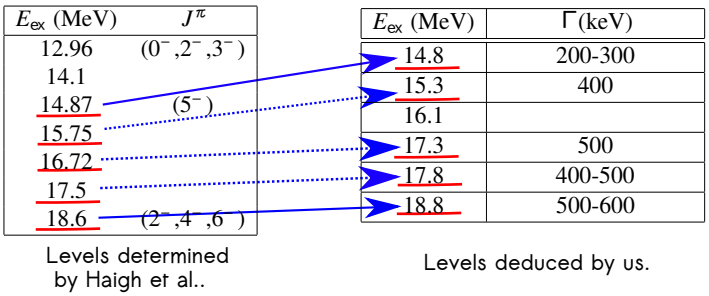

Figure 4.3: Left table shows energies of levels which Haigh et al. determined. Right table shows energies of levels deduced by us. The levels observed by us are pointed with blue arrows from the levels which could correspond. Dashed arrows are used for the levels which do not correspond well.

4.1.2 Comparing values of cross section

If the cross section of Freer et al. and the cross section in the present work are acceptably similar, the parameters which are determined with these excitation function are more reliable. However, the cross section shown in Figure 3.25 is very different from the cross section shown in Figure 4.2. An overlap of the plots is shown in Figure 4.5. The overlap was normalized as the cross sections of the peak at 18.8 MeV have the same value.

The cross section at 18.8 MeV of Freer et al. was around 1.5 b/sr. The cross section at 18.8 MeV in the present work was around 330 mb/sr. If 4 is multiplied to our cross section, the value is 1.3 b/sr, roughly similar to 1.5 b/sr.

E_{ex} (MeV)	J^{π}	Γ(keV)
17.32	3^-	(450, 590)
(17.95, 17.99)	(2^+)	(420, 760)
(18.22)	(4^+)	(200)
18.82	5^-	(500, 590)
19.65	5^-	(100, 140)
20.80	6^+	300

Levels determined by Freer et al..

E_{ex} (MeV)	Γ(keV)
14.8	200-300
15.3	400
16.1	
17.3	500
17.8	400-500
18.8	500-600

Levels deduced by us.

Figure 4.4: Left table shows energies of levels which Freer et al. determined. Right table shows energies of levels deduced by us. The levels deduced by us are pointed with blue arrows from the levels which could correspond.

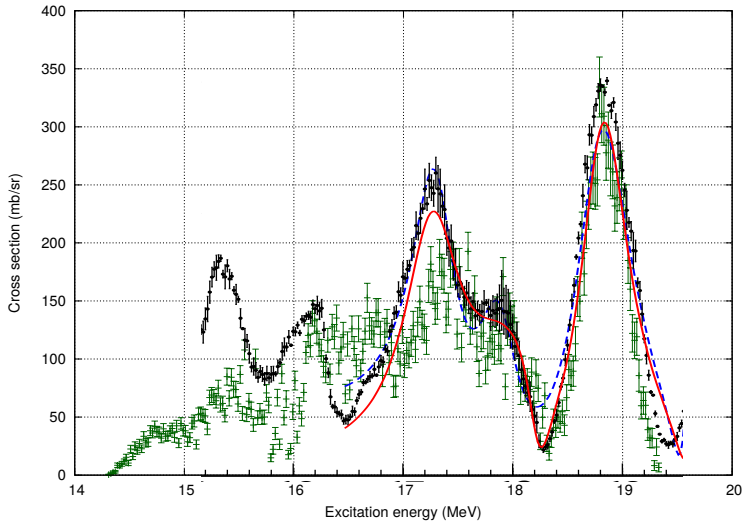

Figure 4.5: Excitation function of Freer et al. overlapped on the excitation function in the present work. The excitation function in the present work is plotted with green points. The excitation function of Freer et al. is plotted with black points. Cross section of Freer et al. at 18.8 MeV was around 1500 mb/sr, while ours was 330 mb/sr. A normalization factor 30/1500=0.22 was multiplied to the cross section of Freer et al.

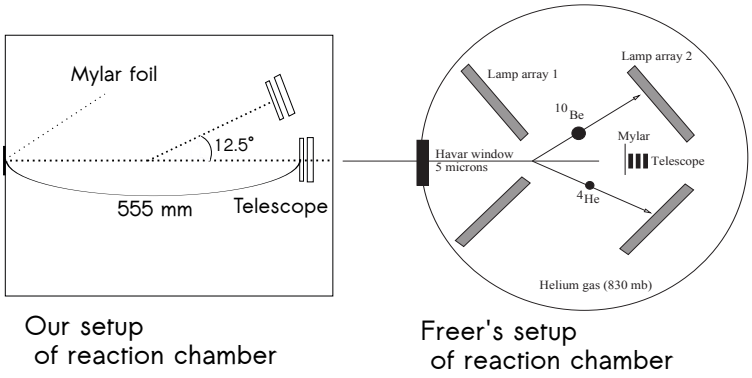

Figure 4.6: Left simplified diagram shows the setup of our reaction chamber. Right diagram shows the setup of Freer's reaction chamber.

Angular region

The range of the scattering angle may explain the difference of the cross section. The mean of the scattering angle in our experiment was 8.1 degrees in laboratory system. The maximum angle in our experiment was 15.2 degrees. Freer et al. insisted that the excitation function was obtained with the telescope which was installed at 0 degrees in laboratory system. Figure 4.6 shows the comparison of the setups in the present work and Freer et al. The distance from the entrance window to the telescope was 38 cm in the experiment of Freer et al. They did not explain the area of the telescope. Though the average angle and the maximum angle depended on the size of the telescope of Freer et al, the angles should be comparable with us.

There is a possibility that the difference of the cross section is caused by the difference of the angle, where the potential scattering has a much higher cross section. In order to generate the cross section over 1000 mb/sr, the scattering angle must be larger than 30 degree in laboratory system in calculation with the LISE++. However the angle of Freer's telescope from the beam line was not possibly larger than 30 degrees by considering the setup of Freer et al. Hence the difference should not be derived from the potential scattering at the large angle.

Considering the resonant scattering is also required for the difference of the whole cross sections between the excitation function of Freer et al. and the excitation function in the present work. Roughly speaking, the cross section of the resonant scattering is proportional to the squared amplitude of the Legendre polynomial function of each angular momentum. The amplitude of the Legendre polynomial function becomes larger if the angle in laboratory system becomes

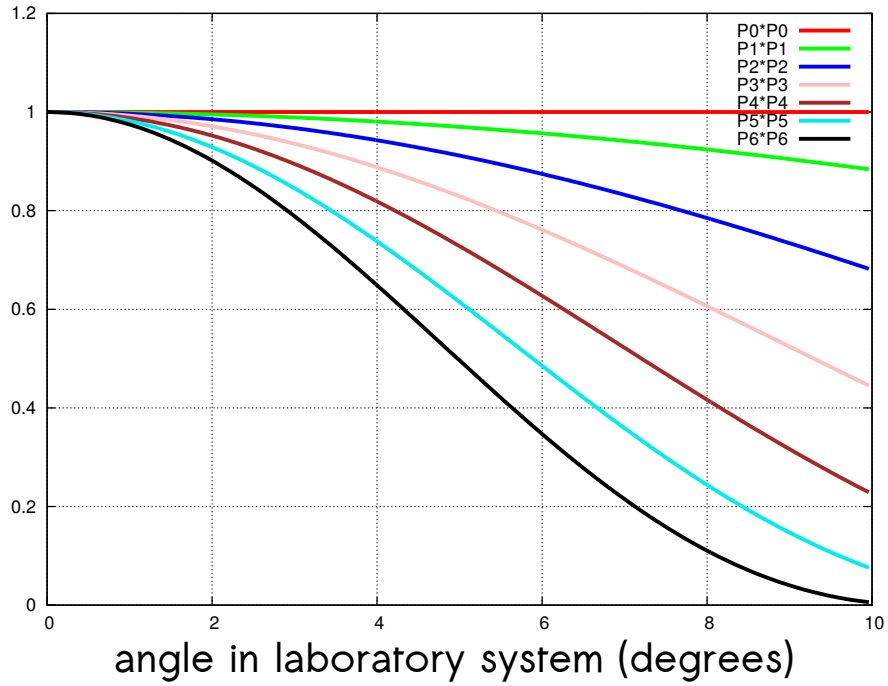

Figure 4.7: Amplitude of the squared Legendre polynomial function versus angle in laboratory system. Red line corresponds to L, angular momentum =0 $\hbar$. Green line corresponds to $L = 1\ \hbar$, blue line $L = 2\ \hbar$, pink line $L = 3\ \hbar$, brown line $L = 4\ \hbar$, cyan line $L = 5\ \hbar$, and black $L = 6\ \hbar$. In this experiment, the angular momentum should be smaller than 6 $\hbar$.

smaller at the region of near 0 degrees as seen in Figure 4.7. If the angle of Freer et al. was smaller than us, the cross section of Freer et al. is larger than ours. However the average angle in the present work was 8.1 degrees in laboratory system, and the cross section does not become 4 times larger than ours however small the angle of Freer et al. was except for the Legendre polynomial functions of which the angular momentum were 5 $\hbar$ and 6 $\hbar$. In addition, the angular momentum of all of the resonances should not 5 $\hbar$ or 6 $\hbar$. Therefore the reason why the whole of the cross section of Freer et al. was 4 times larger than ours should not be the angular difference which creates the larger amplitude of the Legendre polynomial function.

Conversion of systems

The factor of 4 appears when the conversion between laboratory system and center-of-mass system is performed as seen in Subsection 3.7.5. There could be a possibility that the cross section of Freer et al. was not divided by 4 (or $4\cos\theta_{\rm lab}$).

Other factors

There are other factors which could influence the cross section as shown in Section 3.1. The stopping power, the count of yielded α particle and the count of beam particle could be estimated inaccurately in Freer' calculation. There is a possibility that the factor of $m_\alpha/(m_\alpha + m_{\rm Be})$ = 1/3.5 was not multiplied.

4.1.3 Comparing shapes of excitation functions

The shapes of the excitation functions are similar above 17.6 MeV as shown in 4.5. However the shapes are remarkably different under 17.6 MeV. The subtraction of the background could cause the difference of the shapes.

Difference of thickness between He gas and Ar gas

In order to discuss the difference of the shapes between the excitation function of Freer et al. and the excitation function in the present work under 17.6 MeV, considering the subtraction of the background is required.

The measurement of the beam energy was also performed in the Ar gas as seen in Figure 4.8. Figure 4.9 shows the comparison of the beam energies in the He gas and the Ar gas. The beam was stopped at 471 mm from the entrance window in He gas. The value of 471 mm was determined as the value of the polynomial function in Figure 3.3 is 0. The beam was stopped at 482mm from the entrance window in the Ar gas. The difference of the distance is only 11 mm, and

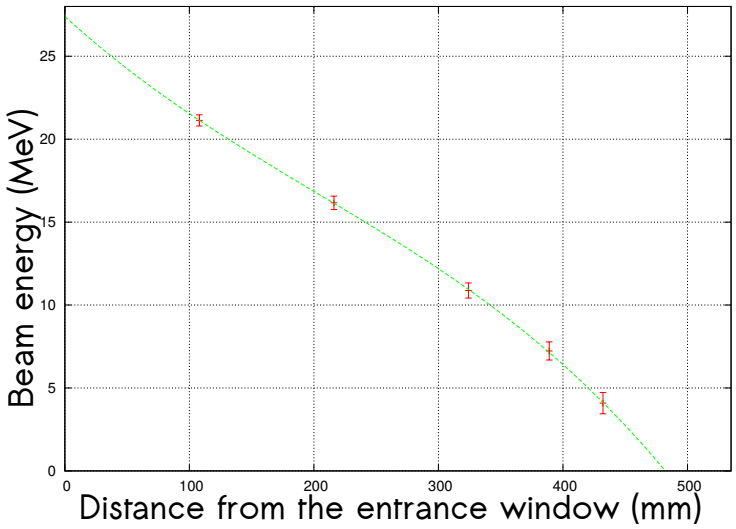

Figure 4.8: Energy of the beam versus equivalent distance from the entrance window in the Ar gas runs. Red points are data points. Green dashed line is a polynomial function fitted to the data points. The gas was Ar for this measurement.

the largest difference of the beam energy at a certain distance from the entrance window in He gas and Ar gas was about 700 keV. The difference of the thickness between He gas and Ar gas was not large for ^{10}Be. It was much smaller for the background α particle, since the energy loss of the background α should be much smaller than ^{10}Be. Therefore the difference of the thickness could not affect the shape of the excitation function very much.

Statistics

There is a possibility that the statistics of our background was low. The shape of the peak at 3.8-4.6 MeV in the histogram in Figure 3.18 is fluctuated because of the low statistics. This fluctuation should cause the fluctuation in the excitation function at 15.9-16.7 MeV.

Determining $E_{\rm cm}$ and the reaction point

We subtracted the background after determining $E_{\rm cm}$ and the reaction point. We did not extrapolate each particle of the beam but the center of the beam. Therefore there was an uncertainty for the determination of the $E_{\rm cm}$ and the reaction point. We subtracted the background after determining the $E_{\rm cm}$ and the reaction point.

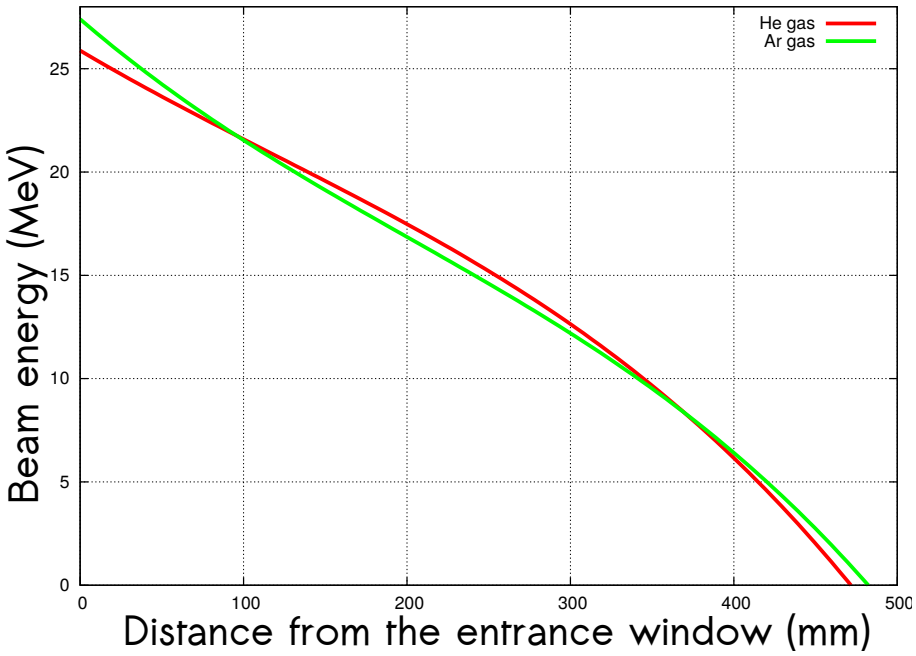

Figure 4.9: Beam energy versus distance from the entrance window in the He gas runs and the Ar gas runs. Red line is a polynomial function fitted with the data points measured at the He gas runs. Green line is a polynomial function fitted with the data points measured at the Ar gas runs.

Hence $E_{\rm cm}$ determined in the He gas runs was different from $E_{\rm cm}$ determined in the Ar gas runs. The difference should cause a disagreement between the bins in He gas runs and the background runs. This should cause the different shapes.

Low $E_{\rm cm}$ corresponded to the long distance from the entrance window. The extrapolation included more uncertainty if the distance was longer. This should also cause the shapes of the peaks at the low energy region in our excitation function wider. This should be reflected to the difference of the shape.

4.2 Linear-chain levels

If the determination of the resonant parameters such as J^π and the α width at these energy region with an R-matrix calculation is performed, precise discussion for the existence of the linear-chain cluster is possible.

Table 4.3 shows linear-chain states in calculation by Suhara & En'yo.

$E_{\rm lin}$ (MeV)	J^π
15.1	0^+
16.0	2^+
19.1	4^+

Table 4.3: Linear-chain states in the calculation by Suhara and En'yo.

There is a possibility that the peaks at 15.3, 16.1 and 18.8 MeV in our excitation function shown in Figure 3.25 are linear-chain levels. If the peak at 15.3 MeV is determined as the resonance of 0^+, the peak at 16.1 as 2^+, and the peak at 18.8 MeV as 4^+ with an R-matrix calculation, the possibility of the existence of the liner-chain cluster states becomes larger.

Freer et al. determined the peak at 18.82 MeV as the resonance of 5^-. However the excitation function of Freer was very different from ours. Therefore the resonant parameters will possibly be determined differently. There is still a possibility of the existence of the linear-chain cluster states in ^{14}C.

Chapter 5

Conclusion

^{10}Be+α elastic resonant scattering experiment was performed with CRIB in May 2015. An excitation function was obtained and compared with previous measurements. The cross section in the present work was very different from the cross section of Freer et al. There could be a possibility that the factor of 4 which was used to convert laboratory system into center-of-mass system was not used for the excitation function of Freer et al.

The shape of the excitation function was similar to the excitation function of Freer et al. above 17.6 MeV. However the shape was different under 17.6 MeV possibly because of the subtraction of the background and the uncertainty of the determination of $E_{\rm cm}$ and the reaction point. We obtained candidates of resonances of linear-chain cluster states.

5.1 Outlook

In order to obtain the excitation function from the angled telescope, determination of the dead layer is necessary. In order to accurately compare the widths of the resonances and the experimental resolution, an evaluation of the experimental resolution should be performed. For concluding whether the linear-chain cluster states exist or not, the determination of the resonant parameters such as J^{π} and α width is required. After obtaining the excitation function with the angled telescope, and obtaining a more accurate excitation function by correcting different $E_{\rm cm}$ between the He gas runs and the Ar gas runs and extrapolating not the center of the beam but each ^{10}Be particle, an R-matrix calculation should be performed for the excitation functions from the centered telescope and the angled telescope in order to determine the resonant parameters.

Acknowledgment

Thanks to the support by my family, I was able to perform this experiment and write this paper. I appreciate it.

I would like to thank my supervisor Prof. Hidetoshi Yamaguchi. He patiently taught me not only physics but also the way how to consider many things. He provided me many chances to grow up to consider and decide by myself. For work of this paper, he kindly provided me many guidances. When I had difficulty which I was not able to solve, he kindly helped me.

I would also like to thank CRIB experts, Dr. Seiya Hayakawa and Dr. David Kahl. Dr. Hayakawa kindly spared a long time to support this experiment. He taught me physics and the analysis many times when I had problems. Dr. Kahl not only supported the experiment but also spared time to write documents to taught me many times. He helped me analyzing a lot. Thanks to their kind help, I was able to make progress.

Dr. Iwasa kindly explained about the method of the analysis during the experiment and cheered me up. Dr. Imai helped me using modules and contributed the online analysis during the experiment. I appreciate it.

I would like to thank other Co-experimentalist.

Students supported this experiment and cheered me a lot. Korean students, especially Dahee and Soomi helped me preparing for the experiment a lot. Soomi gave me a lucky 4-leaf clover before this experiment. I appreciate it.

Thanks to the technical staffs, the preparation of this experiment was proceeded. Thanks to the operators, we performed this experiment. I appreciate it.

I would like to thank all the people who were involved in this experiment and contributed a lot.

Bibliography

[1] H. Morinaga. Interpretation of some of the excited states of $4n$ self-conjugate nuclei. *Phys. Rev.*, 101:254–258, Jan 1956.

[2] Hisashi Horiuchi. Three-alpha model of $^{12}\mathrm{C}$. *Prog. Theor. Phys.*, 51:1266–1268, 1974.

[3] Hisashi Horiuchi. Many-cluster problem by the orthogonality condition model. *Prog. Theor. Phys.*, 53:447–460, 1975.

[4] E. Uegaki, S. Okabe, Y. Abe, and H. Tanaka. Structure of the excited states in ^{12}c. i. *Prog. Theor. Phys.*, 57:1262–1276, 1977.

[5] Y. Fukushima and M. Kamimura. In *Proc. Int. Conf. on nuclear structure*, page 225, Tokyo, 1977.

[6] M. Kamimura. Transition densities between the 0_1^+, 2_1^+, 4_1^+, 0_2^+, 2_2^+, 1_1^- and 3_1^- states in $^{12}\mathrm{C}$ derived from the three-alpha resonating-group wave functions. *Nuclear Physics A*, 351(3):456 – 480, 1981.

[7] K. Kato, H. Kazama, and H. Tanaka. Application of the μ truncation method to 3α orthogonality condition model: Linear-chain structure of 3α and ^{16}o+2α systems. *Prog. Theor. Phys.*, 77:185–189, 1987.

[8] Y. Kanada-En'yo. Variation after angular momentum projection for the study of excited states based on antisymmetrized molecular dynamics. *Phys. Rev. Lett.*, 81:5291–5293, Dec 1998.

[9] A. Tohsaki, H. Horiuchi, P. Schuck, and G. Röpke. Alpha cluster condensation in $^{12}\mathrm{C}$ and $^{16}\mathrm{O}$. *Phys. Rev. Lett.*, 87:192501, 2001.

[10] T. Neff and H. Feldmeier. Cluster structures within fermionic molecular dynamics. *Nuclear Physics A*, 738(0):357–361, 2004.

[11] N. Itagaki, S. Okabe, K. Ikeda, and I. Tanihata. Molecular-orbital structure in neutron-rich c isotopes. *Phys. Rev. C*, 64:014301, May 2001.

[12] N. Itagaki, T. Otsuka, K. Ikeda, and S. Okabe. Equilateral-triangular shape in ^{14}C. *Phys. Rev. Lett.*, 92:142501, Apr 2004.

[13] W. Oertzen, H.G. Bohlen, M. Milin, Tz Kokalova, S. Thummerer, A. Tumino, R. Kalpakchieva, T.N. Massey, Y. Eisermann, G. Graw, T. Faestermann, R. Hertenberger, and H.-F. Wirth. Search for cluster structure of excited states in ^{14}C. *Eur. Phys. J.*, A21:193–215, 2004.

[14] T. Suhara and Y. Kanada-En'yo. *Prog. Theor. Phys.*, 123:303, 2010.

[15] T. Suhara and Y. Kanada-En'yo. *Phys. Rev. C*, 85:054320, 2012.

[16] N. Soić, M. Freer, L. Donadille, N. M. Clarke, P. J. Leask, W. N. Catford, K. L. Jones, D. Mahboub, B. R. Fulton, B. J. Greenhalgh, D. L. Watson, and D. C. Weisser. ^{4}He decay of excited states in ^{14}C. *Phys. Rev. C*, 68:014321, Jul 2003.

[17] M. Milin, S. Cherubini, T. Davinson, A. Di Pietro, P. Figuera, D. Miljanić, A. Musumarra, A. Ninane, A.N. Ostrowski, M.G. Pellegriti, A.C. Shotter, N. Soić, C. Spitaleri, and M. Zadro. The ^{6}He scattering and reactions on ^{12}C and cluster states of ^{14}c. *Nucl. Phys. A*, 730(3–4):285–298, 2004.

[18] D.L. Price, M. Freer, S. Ahmed, N.I. Ashwood, N.M. Clarke, N. Curtis, P. McEwan, C.J. Metelko, B. Novatski, S. Sakuta, N. Soić, D. Stepanov, and V. Ziman. Alpha-decay of excited states in 13c and 14c. *Nucl. Phys. A*, 765(3–4):263–276, 2006.

[19] D. L. Price, M. Freer, N. I. Ashwood, N. M. Clarke, N. Curtis, L. Giot, V. Lima, P. Mc Ewan, B. Novatski, N. A. Orr, S. Sakuta, J. A. Scarpaci, D. Stepanov, and V. Ziman. α decay of excited states in ^{14}C. *Phys. Rev. C*, 75:014305, Jan 2007.

[20] P. J. Haigh, N. I. Ashwood, T. Bloxham, N. Curtis, M. Freer, P. McEwan, D. Price, V. Ziman, H. G. Bohlen, Tz. Kokalova, Ch. Schulz, R. Torabi, W. von Oertzen, C. Wheldon, W. Catford, C. Harlin, R. Kalpakchieva, and T. N. Massey. Measurement of α and neutron decay widths of excited states of ^{14}C. *Phys. Rev. C*, 78:014319, Jul 2008.

[21] M. Freer, J. D. Malcolm, N. L. Achouri, N. I. Ashwood, D. W. Bardayan, S. M. Brown, W. N. Catford, K. A. Chipps, J. Cizewski, N. Curtis, K. L. Jones, T. Munoz-Britton, S. D. Pain, N. Soić, C. Wheldon, G. L. Wilson, and V. A. Ziman. Resonances in ^{14}C observed in the $^{4}\mathrm{He}(^{10}\mathrm{Be},\alpha)^{10}\mathrm{Be}$ reaction. *Phys. Rev. C*, 90:054324, Nov 2014.

[22] F. Ajzenberg-Selove. *Nucl. Phys. A*, 523:1, 1991.

[23] K. P. Artemov, O. P. Belyanin, A. L. Vetoshkin, R. Wolskj, M. S. Golovkov, V. Z. Gol'dberg, M. Madeja, V. V. Pankratov, I. N. Serikov, V. A. Timofeev, V. N. Shadrin, and J. Szmider. Effective method of study of α-cluster states. *Sov. J. Nucl. Phys*, 52:408, 1990.

[24] Y. Yanagisawa, S. Kubono, T. Teranishi, K. Ue, S. Michimasa, M. Notani, J. J. He, Y. Ohshiro, S. Shimoura, S. Watanabe, N. Yamazaki, H. Iwasaki, S. Kato, T. Kishida, T. Morikawa, and Y. Mizoi. Low-energy radioisotope beam separator crib. *Nucl. Instrum. Meth. Phys. Res., Sect. A*, 539:74–83, 2005.

[25] H. Kumagai, A. Ozawa, N. Fukuda, K. Sümmerer, and I. Tanihata. Delay-line ppac for high-energy light ions. *Nucl. Instrum. Meth. Phys. Res., Sect. A*, 470:562, 2001.

[26] W.R.Leo. *Techniques for Nuclear and Particle Physics Experiments*.

[27] H. Baba *et al. RIKEN Accel. Prog. Rep.*, 34:221, 2001.

[28] *ANAPAW*. http://rarfaxp.riken.go.jp/ takesato/anapaw/anapaw.html.

[29] J. F. Ziegler, J. P. Biersack, and U. Littmark. *The Stopping and Range of Ions in Solids*. New York, 1985.

[30] *A simulation of fragment separators*. http://groups.nscl.msu.edu/lise/lise.html.